

# Revisiting gradient wind balance in tropical cyclones using dropsonde observations

Jorge L. García-Franco<sup>a,b\*</sup> and Juliane Schwendike<sup>a</sup>

<sup>a</sup> *School of Earth and Environment, University of Leeds, UK*

<sup>b</sup> *Atmospheric, Oceanic and Planetary Physics, Department of Physics, University of Oxford.*

\*Correspondence to: Clarendon Laboratory, University of Oxford, Parks Road, Oxford OX1 3PU, United Kingdom. E-mail:

jorge.garcia-franco@physics.ox.ac.uk

This study diagnoses the degree of gradient wind balance (GWB) in dropsonde observations of 30 tropical cyclones (TCs) divided into 91 intense observation periods. The diagnosed GWB in these observation periods are composited to investigate which characteristics of a TC are significantly related to departures from GWB. This analysis confirms that on average the flow above the boundary layer is approximately in GWB. Supergradient flow is more common near the radius of maximum wind (RMW) in the upper boundary layer than above in the free troposphere or outside the RMW and is also more common in strong storms than in weak storms. In contrast, the degree of GWB does not differ between intensifying, steady-state and weakening storms. Storms with a peaked wind profile have a higher probability of showing supergradient winds than those with a flat wind profile. The comparison of two commonly used functions to fit observations shows that the diagnosing GWB from dropsonde observations is highly dependent on the analysis technique. The gradient wind magnitude and even sign is shown to depend on which of these functions is used to fit the observations. The use of a polynomial fit consistently diagnoses the presence of supergradient winds far more frequently than a piece-wise function, and also shows a marked degree of imbalance above the boundary layer. Therefore, caution is warranted when determining the degree of GWB with a polynomial fit.

This article has been accepted for publication and undergone full peer review but has not been through the copyediting, typesetting, pagination and proofreading process which may lead to differences between this version and the Version of Record. Please cite this article as doi: 10.1002/qj.3947

## 1. Introduction

Gradient wind balance (GWB) in tropical cyclones (TCs) has long been investigated by observational and modelling studies (e.g. Gray and Shea 1973; Willoughby 1979; Pendergrass and Willoughby 2009; Miyamoto *et al.* 2014) due to the different roles that balanced and unbalanced dynamics have for storm structure and intensification in theoretical and numerical models (Shapiro and Willoughby 1982; Bui *et al.* 2009; Smith and Montgomery 2010; Montgomery and Smith 2017; Heng *et al.* 2017). The first analyses of aircraft data that diagnosed whether the wind was close to GWB found contradictory results because different methodologies would render different conclusions (e.g. Gray 1962; Gray and Shea 1973; Willoughby 1979; Jorgensen 1984).

The debate remained until the influential analysis of Willoughby (1990) concluded that the mid- and low-troposphere of the majority of TCs was in GWB. Although this result was contested by Gray (1991), GWB was considered a fair assumption in TCs and became a common constraint in theoretical TC models, particularly above the boundary layer, for example in the Wind-Induced Surface Heat Exchange (WISHE) model (e.g. Emanuel 1997) or in the Sawyer-Eliassen equation (Pendergrass and Willoughby 2009; Heng *et al.* 2017). However, recent observations have shown that imbalances may occur. In particular, in dropwindsondes, several analyses documented supergradient winds (e.g. Kepert 2006a,b; Schwendike and Kepert 2008; Bell and Montgomery 2008; Montgomery *et al.* 2014, hereafter M14), especially in the upper boundary layer.

The boundary layer model of Kepert (2001) and Kepert and Wang (2001) provides a theoretical framework to explain supergradient winds in the upper boundary layer. In their model, supergradient flow in the upper boundary layer was caused by the strong inward advection of angular momentum, thereby linking the presence of supergradient winds to the radial distribution of angular momentum. Furthermore, Stern *et al.* (2020) recently used an axisymmetric version of the boundary layer model of Kepert and Wang (2001) to explain why the flow right above the top of the boundary layer should be weakly subgradient. Stern *et al.* (2020) argue that the layer of subgradient flow near the eyewall is associated with an inertial oscillation and is strongly influenced by the radius of maximum wind (RMW).

Kepert (2006a,b) found that the degree of GWB in Hurricanes Georges (1998) and Mitch (1998) was a function of the radial shape of the wind profile, which is related to the radial distribution of absolute angular momentum. Although Georges and Mitch had relatively similar intensities, the GWB analysis showed that Georges was close to GWB whereas Mitch showed markedly supergradient flow near the RMW. One of the main differences between Mitch and Georges was the radial gradient of wind speed: while Georges had a smooth flat radial wind profile, Mitch had a peaked profile. These studies argue that the radial shape of the wind profile determines the advection of angular momentum and influence the degree of GWB in these storms, as accounted for by the model of Kepert and Wang (2001).

Schwendike and Kepert (2008) provide further evidence that the shape of the radial wind profile is related to the degree of GWB. They showed that Hurricane Danielle (1998) with relatively weak winds (Cat. 2) and a flat radial wind profile was close to GWB. In contrast, their analysis of Hurricane Isabel (2003), a major hurricane (Cat. 5) with a peaked wind profile, showed strongly supergradient winds in the upper boundary layer and was balanced above 2000 m.

A recent theoretical examination of the validity of GWB arose in the paradigm for TC intensification, known as the boundary layer spin-up mechanism, which proposes that supergradient flow in the boundary layer imports air into the eyewall with minimal loss of momentum (Smith and Montgomery 2010; Montgomery and Smith 2017). The supergradient flow in the boundary layer is advected upwards and acts to directly intensify the vortex (e.g. Smith and Montgomery 2016; Montgomery and Smith 2017).

Observational evidence (see e.g. Montgomery *et al.* 2006; Bell and Montgomery 2008; Bell *et al.* 2012; Sanger *et al.* 2014; Rogers *et al.* 2015; Abarca *et al.* 2016) has supported this theory by documenting supergradient winds in the boundary layer in dropsonde observations. For example, M14 used dropsondes deployed in Hurricane Earl (2014) to diagnose supergradient winds in

40 four observation periods of Earl: two periods where the storm was weak and intensifying, and two periods where Earl was a major  
 41 hurricane and with relatively constant strength. Their results suggest that during the four periods the storm was supergradient near the  
 42 inner-core at the top of the boundary layer. Rogers *et al.* (2015) also shows evidence of supergradient winds for Hurricane Earl near the  
 43 RMW from the surface up to 2400 m. Similar evidence of supergradient winds in the boundary layer of strong TCs was shown for the  
 44 cases of Hurricanes Isabel (2003) (Bell and Montgomery 2008), Rita (2005) (Bell *et al.* 2012), Edouard (2014) (Abarca *et al.* 2016)  
 45 and Typhoon Jangmi (2008) (Sanger *et al.* 2014).

46 The degree of GWB was assessed in the studies mentioned above (e.g. Kepert 2006a; Schwendike and Kepert 2008; Bell *et al.* 2012),  
 47 by analyzing low-level dropsonde observations of the tangential wind and comparing them to an estimation of the gradient wind. To  
 48 estimate the GWB winds, dropsonde observations of pressure (and/or wind) were fitted with a pressure (and/or wind) continuous  
 49 function producing a radial wind profile that was then used to estimate a radial wind speed (or pressure) profile using the gradient wind  
 50 equation. The comparison of these wind (and/or pressure) values estimated through the GWB equation with the observed tangential  
 51 wind (pressure), provided a measure of the degree of GWB.

52 The principal difference between the studies mentioned above was the analytical function used to fit the observations. For example,  
 53 Kepert (2006a) used a piece-wise function (Willoughby *et al.* 2006) whereas Bell and Montgomery (2008) and Didlake and Houze  
 54 (2011) used a polynomial function (see Section 2). While M14 acknowledged that using polynomial fits could be too simplistic, they  
 55 argued that a polynomial function was appropriate since the selection of this family of functions over other functions that they tested  
 56 did not significantly affect the GWB analysis. However, several studies have discussed and shown that the analysis technique may be  
 57 key and potentially a source of error in determining balance in observations (Willoughby 1990; Gray 1991; Kepert 2006a).

58 In short, observational studies have recurrently found supergradient winds in TCs, and several theories and models of intensification  
 59 provide physical accounts for the wind flow to depart from GWB. The observational evidence of imbalances summarised above was  
 60 provided in single case studies. However, the question remains as to how many storms show a departure from GWB or indeed  
 61 which characteristics of a storm are linked to the degree of GWB. For instance, the boundary layer spin-up mechanism argues that  
 62 supergradient winds are an essential component of TC intensification, a feature that is supported by several dropsonde case studies  
 63 (Bell and Montgomery 2008; Bell *et al.* 2012; Sanger *et al.* 2014; Rogers *et al.* 2015). One might reasonably infer from their evidence  
 64 that there would be a relationship between the degree to which the winds are supergradient and the intensification rate, with intensifying  
 65 storms being more likely supergradient in the boundary layer and weakening storms being in GWB or having slight supergradient flow.  
 66 Similarly, the boundary layer model of Kepert and Wang (2001) suggested that the radial distribution of momentum determines the  
 67 location and magnitude of supergradient winds, which is also supported by dropsonde evidence in a handful of cases (Kepert 2006a,b;  
 68 Schwendike and Kepert 2008). A reasonable hypothesis arising from their results is that storms with peaked wind profile will more  
 69 likely show supergradient signatures than storms with a flat wind profile.

70 This study investigates the degree of gradient wind balance in a larger set of TCs and dropsonde observations. The primary  
 71 motivation of this study is to expand on the results from the case studies to quantify whether there is any statistical relation between  
 72 TC characteristics and the degree of GWB. In particular, as explained above, four characteristics of TC structure and development have  
 73 been theoretically linked to GWB: mean intensity, the rate of change of intensity, the height level and the shape of the radial wind  
 74 profile.

75 This paper is structured as follows. Section 2 describes the data and the methodologies used to analyse the GWB and to composite  
 76 the observations. Section 3 shows a few well-known example cases to illustrate and compare existing methods to measure the degree  
 77 of GWB. Section 4 then presents the analysis of the degree of GWB in dropsonde composites. These results are discussed in Section  
 78 5, which also presents the conclusions.

## 79 2. Data and methodology

80 Dropsondes are scientific instruments launched from research aircrafts from the National Oceanic and Atmospheric Administration  
81 (NOAA), the United States Air-Force (USAF), the National Aeronautic and Space Administration (NASA) and by the National  
82 Taiwan University. Since their development, dropsonde observations have been useful for operational and research purposes due  
83 to their unique vertical and horizontal information of the TC inner-core wind and temperature structure (Franklin *et al.* 2003;  
84 Zhang *et al.* 2011, 2013; Wang *et al.* 2015). A large dropsonde dataset, thoroughly described in Wang *et al.* (2015) (obtained from  
85 [www.eol.ucar.edu/content/noaa-hurricane-dropsonde-archive](http://www.eol.ucar.edu/content/noaa-hurricane-dropsonde-archive)), is the main data source of this study.

86 This dataset contains observations taken between 1999-2012 from onboard research flights of NOAA, USAF and NASA research  
87 aircrafts. Each dropsonde profile has been corrected and quality-controlled to account for sensor offsets, the effect of shear on the  
88 sonde, accelerated descent rates and other system failures. The raw dropsonde files have been processed by the Atmospheric Sounding  
89 Processing Environment (ASPEN) which smooths and filters the data, after which most dropsonde profiles were visually evaluated as  
90 further quality control (Wang *et al.* 2015). In order to standardize the analysis, the GWB analysis was done in 100-m intervals from 100  
91 m to the highest recorded level from each profile. The wind or pressure values in this 100-m spacing are obtained by averaging all the  
92 data-points in a 20-m window. Previous studies such as Kepert (2006a,b) and Schwendike and Kepert (2008) accounted for the radial  
93 motion of the sonde and the horizontal temperature gradient. The data in this study has not undergone these corrections. Other than the  
94 vertical averaging to a 100-m interval grid as described above, the dropsonde profiles are only processed by putting the observations in  
95 a storm relative-framework using the tracks described in the following section.

### 96 2.1. Track determination

97 An accurate track can be essential for studies investigating the tangential wind speed in the inner-core (Kepert 2005), particularly in  
98 regard to GWB assessments, due to the sensitivity of the analysis technique to track errors. Flight-level data (Vigh *et al.* 2015), available  
99 at <https://verif.rap.ucar.edu/tcdata/flight/>, provide a track time-series with high temporal resolution. The tracks  
100 in this dataset were estimated using the Willoughby-Chelmow (WC) (Willoughby *et al.* 1982) algorithm, based on flight-level wind data.  
101 The WC method minimises the distance between the centre of the storm and tangential lines to the direction of each wind observation.  
102 This centre-finding method has been extensively used in dropsonde analyses (e.g. Zhang *et al.* 2011, 2013; Rogers *et al.* 2013) due to its  
103 simple interpretation and application, as well as its suitability to be used on high temporal resolution onboard radar wind measurements  
104 (Zhang *et al.* 2011).

105 Although the main track finding algorithm used is the WC, two alternative track datasets were used to analyse the sensitivity of  
106 the GWB analysis technique to the track: the best track dataset (Landsea and Franklin 2013) and the translating pressure fit (TPF)  
107 technique (Kepert 2005). The best-track dataset (Landsea and Franklin 2013) has a 6-h temporal resolution which makes this dataset  
108 less suitable for inner-core studies but it has been extensively used, for instance, to determine the rate of intensity change of a storm  
109 (e.g. Hendricks *et al.* 2010). The TPF method determines the centre as the point that minimizes the error of fitting a profile (Holland  
110 1980) to pressure observations (Kepert 2005).

### 111 2.2. Intense observation periods

112 An intense observation period (IOP) is defined as a finite time-frame where a storm was well-sampled. IOPs have been used previously  
113 (e.g. Rogers *et al.* 2013) to merge observations into a single sample and to evaluate the mean characteristics of a storm during a specific  
114 period. In particular, this study considers an IOP as a period where a given storm had more than ten dropsondes in the inner-core  
115 region ( $r < 100$  km). Similarly, each IOP could be no longer than 12 hours and could not overlap with another IOP. This threshold

constrained the period to avoid artefacts in the analysis caused by intensity or structure changes in the storm. The use of IOPs relies on the assumption that during the IOP, relatively few changes occurred during this time to the storm, which is not always the case. Several studies require that during an IOP the storm is approximately in steady-state (Kepert 2006a,b; Schwendike and Kepert 2008), i.e., that the intensity of the storm does not greatly vary within the IOP. Other studies define IOPs based on the periods in which the storms were well-sampled with particular interest on periods where the storm was undergoing intensity or structural changes such as eyewall replacements (e.g. Abarca *et al.* 2016). In this study, the definition of IOP, as stated above, depends only on length and inner-core dropsonde constraints, to maximize the number of IOPs.

Out of all observations in the dropsonde dataset, over 100 IOPs fulfilled the previous definition. However, only 91 IOPs ( $\approx 3000$  dropsondes) are reported in this study since the GWB analysis of most of the weakest storms (tropical storm strength or weaker) was challenging as in most of these cases the radial pressure gradient was very small which caused the GWB analysis to diagnose unrealistic gradient wind estimations. Table 1 shows the information of each IOP, including storm name, start and end dates of each IOP.

### 2.3. Compositing

The IOPs were composited according to three main characteristics: mean TC intensity, intensity change rate, and the shape of the wind profile. The analysed TCs were classified using the Saffir-Simpson scale based on their mean intensity, i.e., the average was taken of all the intensity values in the best-track dataset reported within an IOP.

The categories of intensity change or rate of intensification of each IOP were determined by computing the rate of change of intensity of the TC during the IOP. Several definitions exist of intensity change (e.g. Hendricks *et al.* 2010; Rogers *et al.* 2013; Cione *et al.* 2013), which measure the rate of change in wind speed reported in the best-track dataset in a given period. Here, as in Hendricks *et al.* (2010), we use the following categories of intensity change: *intensifying* IOPs were defined as  $\Delta I/\Delta t \geq 10 \text{ kt } 24\text{-h}^{-1}$ , *weakening* IOPs as  $\Delta I/\Delta t \leq -10 \text{ kt } 24\text{-h}^{-1}$ , and *steady-state* IOPs as  $-10 < \Delta I/\Delta t < 10 \text{ kt } 24\text{-h}^{-1}$ . For this classification, the best track dataset was first interpolated to 1-h resolution. The change in wind intensity  $\Delta I$  is computed as the difference between the closest time-step in the interpolated 1-h best track dataset to the middle-point of an IOP, and the intensity found 12-h later. Because this difference is computed over a time window of 12-h, the result is multiplied by two to adjust to the criteria above, measured in  $\text{kt } 24\text{-h}^{-1}$ . This final value is then used to classify the IOPs using the definitions above.

Two alternative definitions of intensity change were employed to evaluate the sensitivity of the results to this definition of intensity change categories. One method computes  $\Delta I$  over the subsequent 24-h period instead of over the following 12-h. The other definition computes the change of intensity within the IOP by calculating the difference between the closest intensity in the best track to the start and end times of the IOP, i.e., this metric aims to measure the change of intensity while measurements were taking place.

Finally, the shape of the resulting gradient wind profile at each height was classified as either *peaked* or *flat* by inspecting the fitted wind profile or the derived gradient wind profile as in Kepert (2006a,b) and Schwendike and Kepert (2008). This classification was done using two threshold criteria based on the radial gradient of the wind speed. The first criteria was that peaked profiles have a radial gradient of the wind  $|\partial v/\partial r| > 1 \text{ m s}^{-1} \text{ km}^{-1}$ . In this first criteria, stronger storms have a higher likelihood of being classified as 'peaked', simply because they are stronger and more likely to fit this criteria. Therefore, the second criteria weighs the wind observations by the maximum tangential wind speed ( $V_{max}$ ), as 'peaked' profiles are those that meet the criteria  $\partial \frac{V}{V_{max}}/\partial r > 16 \text{ m}^{-1}$ . These thresholds aim to capture the strength of the radial decrease in wind speed between the RMW and 2RMW. Composites of wind profiles (see Fig. S1) show that these criteria are able to separate wind profiles where the maximum wind decreases more rapidly (peaked) compared to those with a smoother weakening in wind speed (flat) outside the RMW.

Section 3 will present examples of peaked and flat wind profiles illustrating how these threshold are a reasonable estimation of when a profile is peaked or flat. Table 1 also presents the mean intensity  $\bar{I} \text{ (kt)}$  of each IOP, the intensity category on the Saffir-Simpson Scale

155 (I. Cat.), the intensity change rate ( $ICR$   $kt\ 24-h^{-1}$ ), and whether the wind profile was classified as being peaked (P) or non-peaked  
 156 (NP), *i.e.*, flat at the boundary layer top and above.

157 Figure 1 illustrates how the 91 IOPs are distributed between each of the composite categories of intensity and intensity change. The  
 158 largest number of cases in the intensity composite were hurricanes of Category 1. Since the number of *Cat.* 5 hurricanes was low, these  
 159 storms were combined with the *Cat.* 4 storms. The majority of IOPs represent weakening (48 cases) and intensifying (30) storms and  
 160 a relatively low number of IOPs (13) are in the *steady-state* category (Figure 1). Out of the 91 IOPs, 34 (26) showed a *peaked* and 57  
 161 (65) a *flat* wind profile in the boundary layer (above the boundary layer).

#### 162 2.4. Gradient wind balance

163 The gradient wind is defined through the balance of the pressure gradient force by the sum of the centrifugal and the Coriolis force  
 164 (Holton and Hakim 2012), as follows:

$$\frac{1}{\rho_0} \frac{\partial p}{\partial r} = \frac{V_g^2}{r} + fV_g, \quad (1)$$

165 where  $\rho_0$  is the density,  $r$  is the distance to storm centre,  $\partial p / \partial r$  is the radial pressure gradient,  $f$  is the Coriolis parameter, and  $V_g$  is  
 166 the gradient wind.

167 As in many previous studies, the degree of GWB is diagnosed in an axisymmetric framework, therefore, GWB refers here to the  
 168 balance of forces in the azimuthal mean. This assumption is noteworthy as several factors can induce asymmetry in the wind flow  
 169 in different quadrants of the storm. For instance, an otherwise balanced vortex might have an azimuthal wave-number 1 inertia wave  
 170 superimposed, or a motion-induced asymmetry. Hence, due to the limited number of dropsonde observations and the need to account  
 171 for asymmetries, the azimuthal mean assumption is necessary.

172 The degree of GWB is commonly assessed by comparing the observed pressure or wind speeds with those estimated by the gradient  
 173 wind equation. To better quantify the difference between the observed and estimated winds and possible method biases, the departure  
 174 gradient wind balance or agradiant wind ( $V_{ag}$ ) is defined (Kepert 2006a) as the difference between observed azimuthal  $u_\theta$  and  
 175 estimated gradient  $V_g$  winds, *i.e.*:

$$V_{ag} = u_\theta - V_g. \quad (2)$$

176 The agradiant wind ( $V_{ag}$ ) will be used as a quantitative measure of the degree of GWB.

177 For the purpose of diagnosing gradient wind from dropsonde observations, a continuous function is fitted to pressure or wind  
 178 observations (e.g. Kepert 2006a; Schwendike and Kepert 2008; Bell *et al.* 2012). If pressure observations are fitted then the gradient  
 179 wind equation (equation 1) needs to be differentiated, whereas if wind observations are fitted, the gradient wind equation will need to  
 180 be integrated. The fitted continuous function of pressure or wind is then used to solve equation 1 to compute the remaining field, which  
 181 is considered an estimation of the values of the field if the wind flow was in GWB. For instance, M14 fitted a polynomial (degree 2)  
 182 function to pressure observations and then estimated the gradient wind ( $V_g$ ) from the gradient wind equation. Schwendike and Kepert  
 183 (2008) analysed both pressure-to-wind and wind-to-pressure functions by using a piece-wise function defined by Willoughby *et al.*  
 184 (2006), hereafter the WDR function.

185 The polynomial pressure function  $P(r)$  to be fitted, as defined in several studies (e.g. Bell *et al.* 2012), can be written as:

$$P(r) = \sum_{k=0}^n a_k r^k, \quad (3)$$

186 where  $n$  is the degree of the polynomial,  $a_k$  are the coefficients to be determined by the fit, and  $r$  is the distance to storm centre. While  
 187 M14 used  $n = 2$ , Didlake and Houze (2011) used  $n = 6$  and Bell *et al.* (2012)  $n = 3$ . Tests using different  $n$  values from 2 to 6 showed  
 188 that increasing  $n$  often leads to overfitting and critical poor fits, especially when no dropsondes are found outside the 100 km radius to  
 189 constraint the polynomial. For this reason, in this study  $n = 3$  is used.

190 WDR showed that a piece-wise function provided more realistic radial pressure gradients and radial wind profiles than previously  
 191 used profiles (e.g. Holland 1980). The WDR function was defined as a wind function over three regions: the inner, transition,  
 192 and the outer region. The inner region wind profile  $V_i(r)$  is defined between the storm centre and the RMW, *i.e.*, in the interval  
 193 ( $0 \leq r \leq RMW$ ).  $V_i(r)$  is given by the following:

$$V_i(r) = V_{max} \left( \frac{r}{RMW} \right)^n, \quad (4)$$

194 where  $V_{max}$  is the maximum tangential wind and  $n$  is an exponent to be fitted to the data. In the outer region, the wind profile  $V_o(r)$  is  
 195 the sum of two weighted-functions with different length scales:

$$V_o(r) = V_{max} \left[ (1 - A)e^{-\frac{r-RMW}{L_1}} + Ae^{-\frac{r-RMW}{L_2}} \right], \quad (5)$$

196 where  $L_1$  and  $L_2$  are e-folding distances, and  $A$  is a relative weight of  $L_1$  and  $L_2$ .

197 Finally, the wind profile in the transition region  $V_{tz}$ , for  $R_1 \leq r \leq R_2$  is a linear combination of equations 4 and 5, given by:

$$V_{tz}(r) = V_i(1 - w) + V_o w, \quad (6)$$

198 where  $w$  is a polynomial of degree 9. See Kepert (2006a), Willoughby *et al.* (2006) and Schwendike and Kepert (2008) for further  
 199 details.

200 The fit of the WDR function follows closely the method outlined in Kepert (2006a) and Schwendike and Kepert (2008) as the  
 201 pressure version of the WDR wind fit is found by radially integrating the gradient wind equation using the WDR wind function.  
 202 However, there are relevant differences from these previous studies in the fit optimization technique and approach as follows.

203 The pressure version of the WDR function was fitted to the pressure observations from the dropsonde profiles every 100-m using  
 204 non-linear squares optimization technique in three steps. The minimum and maximum values of these parameters for this fitting  
 205 procedure are shown in Table 2. The first step is to fit the inner region observations to the inner region pressure profile using equation  
 206 4 which results in fitted values of  $V_{max}$  and  $RMW$ . Using the  $V_{max}$  and  $RMW$  from the best fit in the inner region, the outer region  
 207 observations are fitted to the outer region pressure function to estimate  $A$ ,  $L_1$  and  $L_2$ . In short, step 1 and 2 constrain  $V_{max}$ ,  $RMW$   
 208 and  $A$ . The third and final step then fits the pressure observations simultaneously in the inner, outer and transition regions holding  
 209  $V_{max}$ ,  $RMW$  and  $A$  fixed from the values obtained by the previous steps to produce a continuous pressure profile. This profile is then  
 210 iteratively optimized to find the values of  $n$ ,  $L_1$  and  $L_2$  that produce the best fit across all the observations. In other words, the final  
 211 step optimizes a fit of the optimized individual fits per region using the constraints given by the first two steps. The gradient wind  $V_g$  is  
 212 then obtained by numerically solving the gradient wind equation (equation 1) using the fitted pressure profile (either the polynomial or  
 213 the WDR function) via a numerical quadrature method.

### 214 3. GWB Analysis of Selected IOPs

215 This section illustrates the GWB analysis techniques by comparing the results from the two fitting functions for previously analysed  
 216 well-sampled storms. For each IOP, the two pressure-versions of the fits were adjusted to the pressure observations, and then, the

217 pressure profiles were used to compute the gradient wind ( $V_g$ ). The residual is the difference between the fitted pressure function  
 218 estimate and the pressure observations, which is often used to evaluate the skill of each fit.

219 The first case is that of Hurricane Earl (2010). Two IOPs of Earl are shown, the first period corresponds to 18 UTC 30 August to 01  
 220 UTC August 2010 (IOP 71 from Table 1) and the second to 06-18 UTC on 2 September, 2010 (IOP 75). Earl was an Atlantic hurricane  
 221 that went through a period of rapid intensification and was very well-sampled (Braun *et al.* 2013). The degree of GWB of Earl was  
 222 analysed in 4 IOPs in M14, who used the polynomial fit (degree 2). Earl underwent rapid intensification during the former two IOPs,  
 223 reached peak intensity and was a mature storm in a relative steady-state during the latter two IOPs. M14 found a difference between  
 224 observed winds and the estimated gradient winds of 20 – 60%, *i.e.*, evidence of supergradient wind flow at the height of maximum  
 225 tangential wind speed.

226 The first example (IOP 71) falls between the second and third IOPs of M14 and the second example shown here corresponds to the  
 227 fourth period analysed in M14. Figure 2a, b show the pressure observations and the two continuous pressure profiles for the first case,  
 228 Figure 2c, d show the residual, which is the difference between the fits and the observations, and Figure 2e, f show the gradient wind  
 229 from both fitting methods. Figure 2a, b highlights the differences between the polynomial pressure function and the WDR pressure  
 230 function, particularly in the shape of the pressure profile. Figure 2e, f show differences in the shape and magnitude of the gradient wind  
 231 profile. Although the magnitude of the residuals is very similar (Figure 2c, d), the polynomial residuals are mostly positive outside of  
 232 the 50 km radius, suggesting that the fit misses the data outside the RMW. The WDR fit does not have this problem. Another relevant  
 233 difference between the methods is the shape of the fitted pressure profiles which determines the radial gradient of pressure.

234 Since the gradient wind equation refers to the radial gradient of pressure, the resulting gradient wind estimations  $V_g$  have different  
 235 shapes and RMW locations. The polynomial  $V_g$  estimates the RMW to be in the outer region of the storm, far away from the observed  
 236 RMW, whereas the WDR  $V_g$  produces an RMW very close to the observed value. M14 argued that the misrepresentation of the RMW  
 237 location (of the polynomial  $V_g$ ) was further evidence of the “inaccuracy of the gradient wind for characterizing the structure of the  
 238 vortex”. However, Figure 2 suggests that some of the results presented by M14 were an artefact of the method and not indicative of  
 the degree of GWB, for instance, the location of the RMW. A qualitative assessment of the polynomial  $V_g$  suggest that this IOP was  
 supergradient in the inner-core both at the 600-m level and above. The two methods disagree on the degree of GWB as the WDR fit  
 241 suggests a flow close to balance at both levels in the inner-core.

242 Figure 3 shows the results for a second example IOP of Hurricane Earl (IOP 75), which can be compared to Figure 11 and 12  
 243 of M14. The RMW is located in different regions depending on the fit and the flow near the centre of the storms can be classified  
 244 as supergradient by the polynomial fit but is closer to balance by the WDR function, as was the case in the previous example. The  
 245 mean gradient wind anomaly was estimated for each level and weighted by the maximum wind speed to render a percentage value.  
 246 The reported 32% supergradient wind by M14 for this period is confirmed and also reduced to less than 10% in the estimate by the  
 247 WDR function. A qualitative assessment of both the WDR and the polynomial  $V_g$  suggest that this IOP had supergradient winds in the  
 248 azimuthal mean in the boundary layer, although by noticeable different magnitudes. Very similar features were observed in the analysis  
 249 of the remaining nine periods of Hurricane Earl (see Table 1). Three of these periods were also analysed by M14, who diagnosed  
 250 supergradient winds in these periods in the inner-core across the boundary layer but also at the 2000-m level (see their Figure 12).

251 Hurricane Rita (2005), another well-studied storm, experienced an eyewall replacement cycle that modified the storm structure and  
 252 intensity (see e.g. Rogers and Uhlhorn 2008; Judt and Chen 2010). Didlake and Houze (2011) and Bell *et al.* (2012) used the polynomial  
 253 fit ( $n = 6$ ) to analyze the degree of GWB of Rita using dropsonde observations and concluded that Rita had supergradient winds in the  
 254 boundary layer. Figure 4 shows the pressure functions, residuals and  $V_g$  calculations for both the polynomial and WDR functions for  
 255 IOP 44 (Table 1). As for Hurricane Earl, the residuals from the fits are of similar magnitude, but the residuals for the polynomial fit are  
 256 mostly positive for radii between 50 and 90 km, whereas the residuals for the WDR fit appear evenly distributed across the abscissa.

257 Figure 4e, f suggest that the flow is supergradient in and above the boundary layer near the RMW for both fitting methods, although  
 258 noticeably the imbalance is much larger for the polynomial fit. However, the magnitude of the difference between the estimated  $V_g$  and  
 259 the observations is much larger for the polynomial fit than for the WDR function. This lack of agreement between both methods further  
 260 motivates the notion that the degree of diagnosed GWB, particularly in magnitude, is very sensitive to the method used.

261 For instance, another well-studied storm, Hurricane Isabel (2003), showed strong boundary layer winds (Montgomery *et al.* 2006;  
 262 Bell and Montgomery 2008) and was diagnosed as supergradient in the boundary layer using the WDR fit (Schwendike and Kepert  
 263 2008). The  $V_g$  and  $V_{ag}$  from both fits are shown in Figure 5 during 16-21 h UTC on 12 September, 2003 (IOP 20 from Table 1). The  $V_{ag}$   
 264 (Fig. 5c, d) suggests that Isabel had supergradient winds, *i.e.*, several  $V_{ag}$  observations of over  $+40 \text{ m s}^{-1}$ , according to the polynomial  
 265  $V_g$ . In fact, the mean  $V_{ag}$  found for the polynomial  $V_g$  was  $+24 \text{ m s}^{-1}$  and  $+20 \text{ m s}^{-1}$  for the 600 and 1800-m levels, respectively.

266 The  $V_{ag}$  obtained from the WDR  $V_g$  also shows highly supergradient winds; however, the magnitude of  $V_{ag}$  is different from the  
 267 polynomial results. While some of the resulting  $V_{ag}$  from the WDR  $V_g$  are over  $+20 \text{ m s}^{-1}$ , the mean  $V_{ag}$  is  $+8 \text{ m s}^{-1}$  and  $+2 \text{ m s}^{-1}$   
 268 for the 600 and 1800 m, respectively. Welch t-tests showed that the resulting gradient wind anomalies  $V_{ag}$  of the two methods were  
 269 significantly different from each other at the 99% confidence level at both 600 and 1800-m levels. Furthermore, the resulting  $V_{ag}$  mean  
 270 anomalies from the polynomial fit were significantly different to 0 at the 99% confidence level at both 600 and 1800 m, whereas the  
 271 anomalies resulting from the WDR fit were only significant at the 600 m level to the 95% confidence level.

272 The results of the WDR function support the conclusion of Schwendike and Kepert (2008) that the flow in the upper boundary layer  
 273 near the RMW was supergradient whereas the flow outside the RMW and above the boundary layer was in balance. This conclusion  
 274 changes depending on the method. While the polynomial fit suggests that the flow is supergradient at all height levels near the RMW,  
 275 the results from the WDR function show that the supergradient winds were observed only in the upper boundary layer (600 m).

276 The polynomial fit more frequently diagnosed supergradient winds, *i.e.*, typically larger and positive  $V_{ag}$  were diagnosed using the  
 277 polynomial fit compared to the WDR fit, not just for the cases of Earl and Rita but consistently for most of the analysed IOPs. For  
 278 example, IOP 13 (see Table 1) of Hurricane Michelle (2001), shown in Figure 6, illustrates the different gradient wind anomalies  
 279 resulting from each method. Figure 6a, b shows the wind observations and gradient wind profiles diagnosed from the polynomial and  
 280 WDR fits. The polynomial fit has an overall positive  $V_{ag}$  both at the 600 and 1800-m levels, whereas the WDR fit shows a balanced  
 281 flow in the upper boundary layer and a weakly subgradient flow above (Figs. 6c, d). These differences in the gradient wind anomalies  
 282 between the methods were determined to be statistically significant at 600 m at the 95% confidence level by a Welch t-test, but the  
 283 differences are not significant at the 1800-m level.

284 To illustrate the difference between *peaked* and *flat* wind profiles and their relevance to determine the degree of GWB, Figure 7  
 285 shows the wind profiles of IOPs 80, 37 and 31 for Hurricanes Hilary (2011), Frances (2004) and Ivan (2004), respectively. The radial  
 286 gradient of the wind in and above the boundary layer, classified each of these IOPs in distinct categories as explained in section 2.3.  
 287 The WDR wind profile is used to highlight the difference between the wind profiles given this method's superior skill in accurately  
 288 depicting wind profiles. Hurricane Hilary (Fig. 7a, b) was a storm with a peaked wind profile at the top of the boundary layer and a flat  
 289 wind profile above (1600 m); such cases are referred to as "mixed cases". Hurricanes Frances and Ivan illustrate a flat and a peaked  
 290 wind profile, respectively, both in and above the boundary layer. The wind profile of Frances (Fig. 7c, d) shows a small decrease in  
 291 wind speed outside of the RMW, *i.e.* the radial gradient of wind speed outside the RMW is small compared to the same metric for Ivan.  
 292 Consider, for example, the wind speeds in Figure 7c, d at radii 30 and 75 km which are  $\approx 55$  and  $40 \text{ m s}^{-1}$ , *i.e.*, in a 25 km radial  
 293 distance, the wind speed changed by only  $\sim 15 \text{ m s}^{-1}$ . In contrast, a similar measure (wind speed at 40 and 60 km) for Ivan (Figure 7e,  
 294 f) showed a decrease in wind speed of nearly  $20 \text{ m s}^{-1}$  over a shorter distance. This strong contrast in the radial gradient of the wind  
 295 speed is the main difference between flat profiles (Hurricane Frances in Fig. 7c, d) and peaked wind profiles (Hurricane Ivan in Figure  
 296 7e, f). Another example of a peaked wind profile was shown in Figure 4e, f.

297 **4. Composite analysis**

298 This section expands on the previous results by analysing the composites from the 91 IOPs. These composites refer to IOPs separated  
 299 by i) mean intensity, ii) intensity change rate, and iii) the shape of the wind profile, as explained in the methods section. In addition, the  
 300 composites were separated by the height of the measurement to analyze whether the degree of GWB changes depending on the vertical  
 301 layer, for instance, whether supergradient wind is more likely to be diagnosed in the boundary layer than in the free troposphere. Given  
 302 that the WDR method represents the shape of wind profiles best, results in this section mostly show the  $V_g$  and the  $V_{ag}$  computed from  
 303 the WDR pressure function. As in the previous sections, the gradient wind anomalies  $V_{ag}$  are calculated based on the azimuthal mean  
 304 wind in an axisymmetric framework.

305 Probability density functions (PDFs) of the  $V_{ag}$  are used to summarize the differences between the composites. PDFs are useful  
 306 in this instance since they convey information on the distribution of the  $V_{ag}$  from each composite, thus highlighting the mean and  
 307 spread of the difference between the observed wind and the diagnosed gradient wind. Figure 8 shows the PDFs of the diagnosed  $V_{ag}$   
 308 composited based on four characteristics: a) intensity, b) rate of intensification, c) shape of wind profile, and d) height. Similarly, Table  
 309 3 reports the mean and standard deviation of each composite, as well as the likelihood of showing markedly supergradient and markedly  
 310 subgradient flow. These probabilities were estimated by integrating the density function using a trapezoid numerical method. The mean  
 311 of all the diagnosed  $V_{ag}$  for all heights is  $1 \text{ m s}^{-1}$  (Table 3), which confirms the results of Willoughby (1990) that GWB is generally a  
 312 good assumption for the flow of TCs. Alternatively to PDFs, Figures S2 and S3 show the same distributions in the form of cumulative  
 313 density functions and boxplots, respectively, both of which agree well with the PDF analysis that follows.

314 The PDF of all of the observations in the inner-core ( $RMW/2 < r < 3RMW/2$ ), *i.e.*, 16,000 dropsonde observations, is labelled  
 315 *Control* to illustrate the distribution of the gradient wind anomalies  $V_{ag}$  of the 91 IOPs. This distribution shows that gradient wind  
 316 anomalies are roughly evenly distributed across negative and positive anomalies. The *Control* PDF is relatively broad because this  
 317 sample contains observations from multiple height levels, different storms sizes and intensities, all of which may produce a number of  
 318 positive and negative gradient wind anomalies. Additionally, this PDF is evenly distributed due to observational errors, turbulence and  
 319 other factors that affect the dropsonde measurements, as well as possible storm asymmetries between storm quadrants.

320 Figure 8a indicates that stronger storms have a higher probability of experiencing supergradient flow. The PDFs of the Cat. 3, 4 and  
 321 5 TCs suggest a more frequent occurrence of  $V_{ag} > 10 \text{ m s}^{-1}$ , when compared to the *Control* and to weaker storms. Table 3 shows  
 322 that the stronger the tangential wind in an IOP the higher the likelihood of finding markedly supergradient winds in the inner-core. The  
 323 narrowest distribution of all composites is from the weakest composite, *i.e.*, the Tropical Storms and Tropical Depressions (TS/TD),  
 324 which is also the composite with the lowest standard deviation (Table 3). A narrower distribution is interpreted as being more frequently  
 325 in balance.

326 The PDF of the TS/TD category shows the highest probability of gradient wind anomalies in the  $0\text{-}5 \text{ m s}^{-1}$  interval, which suggests  
 327 a balanced flow with a tendency towards very frequent small positive gradient wind anomalies. This relatively narrower PDF is due to  
 328 smaller wind speeds in IOPs in the TS/TD category ( $17\text{-}32 \text{ m s}^{-1}$ ), which are usually observed with weaker radial pressure gradients  
 329 and therefore weaker diagnosed gradient winds compared to stronger storms. Since both the observed and gradient winds are small,  
 330 the resulting gradient wind anomaly is frequently also small.

331 The inner-core observations were composited based on the observed rate of intensification as explained in section 2.3, into  
 332 *steady-state*, *weakening* and *intensifying* IOPs, shown as PDFs in Fig. 8b. The major difference amongst these categories is that  
 333 the *weakening* composite shows a higher likelihood of modest supergradient winds than *steady-state* and *intensifying* IOPs. Table 3  
 334 shows quantitatively that the highest probability of supergradient flow  $p(V_{ag} > 15 \text{ m s}^{-1})$  is that of the *weakening* composite. The  
 335 other difference is that the PDF of the *steady-state* composite has a higher probability of diagnosing weakly subgradient flow than in  
 This article is protected by copyright. All rights reserved.

the other categories. The *intensifying* PDF is very similar to the *Control* PDF and the probabilities of marked sub- and supergradient imbalances are also similar to that of the *Control* (see Table 3).

The gradient wind anomalies  $V_{ag}$  in the inner-core composite based on the shape of wind profile show substantial differences in the PDFs (Fig. 8c) using the criteria of  $|\partial v/\partial r| > 1 \text{ m s}^{-1} \text{ km}^{-1}$ . The PDFs indicate a higher likelihood of supergradient flow in the *peaked* wind profiles when compared to the *flat* profiles and control samples. For instance, consider the probability of  $V_{ag} > 15 \text{ m s}^{-1}$  for the *peaked* and *flat* profiles in Table 3. The probability of the *peaked* composite to have markedly supergradient flow is twice as high than that of the *flat* composite. These results do not change when applying the second criteria  $\partial \frac{V}{V_{max}}/\partial r$  used to account for strong storms (see Figure S4).

The effect of height on the characteristics of the PDFs is shown in Fig. 8d, with observations binned into 4 different categories. The greatest probability of supergradient flow ( $V_{ag} > 10 \text{ m s}^{-1}$ ) is found for observations in the upper-boundary layer (400-600 m) whereas observations close to the surface ( $<400 \text{ m}$ ) show a higher probability of having subgradient flow  $V_{ag} < -10 \text{ m s}^{-1}$ , consistent with the effects surface friction. Gradient wind anomalies above 1500 m appear to have a higher likelihood of presenting weak subgradient flow than at other heights and than the *Control*.

Figure 9 shows the distributions of gradient wind anomalies further divided by both the height and radial location of the dropsonde observation. First, Figure 9a shows that observations in the upper boundary layer near and inside the RMW have a higher likelihood of being supergradient than observations outside the RMW. The PDF of observations outside the RMW is also narrower than the *Control* suggesting that the wind is more likely to be balanced in this region.

Second, Figure 9b, c show the PDFs from observations in the inner-core of strong Cat. 4-5 (Fig. 9b) and weak Cat. 1-2 IOPs (Fig. 9c) at two different height levels: the upper boundary layer (400-600 m) and above 1500 m. These PDFs show that the degree of GWB varies depending on both the intensity of the IOP and the height of the measurement. These PDFs are compared against observations from the *Control* PDF subdivided into two PDFs according to the height level: 400-600 and above 1500 m. Strong storms have a higher likelihood of supergradient wind in the upper boundary layer than above and a higher likelihood of supergradient winds than the *Control* at the same height. Weak storms also show more frequently supergradient winds in upper boundary layer than above 1500 m, however, the likelihood of markedly supergradient winds in Cat. 1-2 IOPs in the upper boundary layer is smaller than that of the *Control* and of stronger storms at the same height. The PDF of the Cat. 1-2 IOPs at the upper boundary layer shows a bimodal distribution with two peaks: a peak in the very weak subgradient region and another peak showing increased probability of modest supergradient flow ( $5 < V_{ag} < 12 \text{ m s}^{-1}$ ).

Furthermore, Figure 9d-f show the observations subsampled by rate of intensification and height. The *weakening* and *intensifying* composites show a higher likelihood of markedly supergradient winds in the upper boundary layer than above 1500 m (Figs. 9d, e). In contrast, the *steady-state* composite shows a slightly narrower PDF in the upper boundary layer than above 1500 m, suggesting a slightly lower probability of supergradient winds in the upper boundary layer than above. The *weakening* composite shows a slightly higher probability of markedly supergradient flow ( $V_{ag} > 15 \text{ m s}^{-1}$ ) than the *Control* and the *intensifying* PDFs in the upper boundary layer. The *steady-state* PDF in the boundary layer top also shows a bimodal structure in the same regions as the Cat. 1-2 PDF of Fig. 9c.

Table 3 presents the results of a Welch t-test between each composite and the *Control* sample, indicating significance at the 95% and 99% levels. Moreover, to statistically test the differences between each PDF, a Kolmogorov-Smirnov (KS) test was used, which measures how likely is a distribution, or a PDF, to be simply a sub-sample of another distribution. In other words, this test evaluates whether a given composite is statistically are distinct from all the observations. Both tests show that the rate of intensity change has the least significant values when compared to the *Control* sample, *i.e.*, this characteristic was the least important to distinguish the degree

375 of GWB amongst composites. In contrast, the peaked wind profiles and the composites of periods of higher intensity were significant  
 376 using both the Kolmogorov-Smirnov and the Welch t-test at the 99% significant level.

377 Given the sensitivity of the  $V_{ag}$  to the different GWB analysis techniques, it is relevant to illustrate how the  $V_{ag}$  PDFs depend on  
 378 the use of the polynomial fit or the WDR function. Figure 10 compares the PDF of the polynomial  $V_{ag}$  with the WDR function for all  
 379 observations. The WDR curve is the same as the one labelled *Control* in previous figures. The choice of function to fit observations  
 380 has a stronger impact over the  $V_{ag}$  anomaly PDF than compositing the observations by any of the characteristics previously used (e.g.  
 381 intensity). For instance, consider the probability of a  $V_{ag} > 20 \text{ m s}^{-1}$  for both methods. The polynomial fit shows a higher probability,  
 382 visible as the large extent of the right tail of the distribution with significant probabilities. The wind speed that correspond to the 99%  
 383 percentile of the distributions is  $28 \text{ m s}^{-1}$  for the WDR fit and  $52 \text{ m s}^{-1}$  for the polynomial fit. This behaviour is much less apparent  
 384 on the left-hand tail, where the distributions are more similar, thus confirming a positive bias of the polynomial fit when compared to  
 385 the WDR functions. The more frequent supergradient winds estimated by the polynomial fit confirm the results of the previous section,  
 386 which suggested that the polynomial fit produced stronger supergradient features when compared to the WDR function.

387 To test the sensitivity of the results to the track dataset used,  $V_{ag}$  was computed using two alternative track datasets (best-track and  
 388 TPF) for ten IOPs (6, 20, 21, 22, 39, 40, 41, 42, 43 and 56). The observations resulting from these alternative tracks were analysed  
 389 using the two fitting functions as for the WC track. The results of each track for each fitting function were compared in different radial  
 390 regions: inside, near and outside the RMW. Boxplots (Figure 11) show that the three datasets produce a very similar mean  $V_{ag}$ . The  
 391 TPF technique produces a larger spread in  $V_{ag}$ , particularly near the RMW. However, the impact of the fitting method on the diagnosed  
 392 gradient wind anomalies  $V_{ag}$  is stronger than the track dataset used to locate the dropsondes in a storm-relative framework. The mean  
 393  $V_{ag}$  using the polynomial fit (Figure 11b) is higher than the results for the WDR function (Figure 11a), regardless of the track method  
 394 and especially near the RMW. The PDFs calculated from the two alternative tracks did not show substantial differences. In particular,  
 395 the mean and spread of each distribution was not significantly different between the track algorithms.

396 Similarly, to analyze whether the definition of intensity change affected the findings of this section, two alternative definitions of  
 397 intensity change were implemented (see method section). One definition is based on the change in wind speed in a 24-h period and  
 398 the other definition considers the difference in intensity during the course of the IOP. The PDFs of the intensity change composites  
 399 using the two alternative definitions of intensity change (not shown) were consistent with the results from the first definition, shown in  
 400 Figures 8 and 9, *i.e.*, no difference between the *intensifying*, *weakening* or *steady-state* composites. The analysis of the PDFs and the  
 401 Welch and Kolmogorov-Smirnov statistical tests showed no sensitivity to the definition of intensity change category.

## 402 4. Summary and discussion

403 Observations of supergradient winds in TCs have been documented in several case studies, but the question remains as to whether  
 404 the degree of GWB is consistently linked to some characteristics of a TC such as intensity. This study expands on previous work by  
 405 diagnosing the degree of GWB in a sample of 91 IOPs corresponding to 30 TCs in the period of 1999-2012.

406 Previous studies have used two different functions to fit pressure observations and then diagnose GWB, some studies use the WDR  
 407 piece-wise function and others use the polynomial function. The two fitting methods were compared for several cases, first by evaluating  
 408 the skill of the fit in reproducing the main features of the radial pressure gradient and, second, by comparing the diagnosed gradient  
 409 wind from both methods to the observed tangential wind. This analysis showed that the diagnosed gradient wind profiles were notably  
 410 different between the polynomial and the WDR functions. Several characteristics of the diagnosed gradient wind profile were sensitive  
 411 to the fitting function such as the location of the RMW and the maximum wind speed. For example, in two IOPs of Hurricane Earl  
 412 and one IOP of Hurricane Rita, the polynomial function resulted in mostly positive residuals in the pressure fit outside 50 km radius, a

413 displaced RMW and a gradient wind much weaker than the observed wind. The WDR fit, in contrast, showed a better representation  
414 of the radial pressure gradient and a more accurate depiction of the RMW compared to observations.

415 In two example IOPs of Hurricane Earl, the polynomial fit diagnosed strongly supergradient winds in the inner-core both at the top of  
416 the boundary layer and above, in agreement with M14. However, the WDR fit diagnosed a balanced flow in the first case (IOP 72) and  
417 a weakly supergradient flow in the second case (IOP 75). For the case of Hurricane Isabel, the polynomial fit diagnosed supergradient  
418 winds in the inner-core at the 600-m and 1800-m levels. The WDR fit, in turn, only diagnosed supergradient winds at the upper-  
419 boundary layer level and not above, as also previously shown by Schwendike and Kepert (2008). The magnitude of the supergradient  
420 winds in the boundary layer was also markedly different between the methods, as the polynomial fit diagnosed the greatest imbalance.  
421 The degree of GWB, quantitatively measured as the difference between the observed winds and the estimated gradient winds, could  
422 differ between using a polynomial and a piece-wise fitting function by more than  $40 \text{ m s}^{-1}$  for individual observations and a mean  
423 anomaly difference between the methods of  $20 \text{ m s}^{-1}$  for some storms.

424 The polynomial fit frequently diagnosed supergradient winds in the upper-boundary layer and above in other storms, such as  
425 Hurricanes Michelle and Rita, which agrees well with previous analyses using the polynomial fit (Bell and Montgomery 2008; Rogers  
426 and Uhlhorn 2008; Rogers *et al.* 2015). Above the boundary layer, the polynomial fit also consistently suggests supergradient winds  
427 (Fig. 10) whereas the WDR more frequently diagnoses a flow closer to balance (observed as a narrower PDF). Also, the RMW  
428 diagnosed from the gradient wind resulting from the polynomial fit occurs at larger radii than observed whereas the WDR fit usually  
429 finds a RMW much closer to the observed RMW.

430 These differences amongst methods reinforce the conclusion that the diagnosis of GWB in observations is highly sensitive to the  
431 technique, in this case the function used for the fit to pressure observations (Gray and Shea 1973; Willoughby 1990; Gray 1991). Given  
432 the better performance of the WDR function in representing observed wind profiles (Willoughby *et al.* 2006), arguably, the results  
433 from the WDR function are more representative than those of the polynomial fit. For instance, the results from the WDR profile are  
434 consistent with our theoretical expectation that the azimuthal mean flow above the boundary layer should usually be relatively close to  
435 GWB.

436 Additionally, this study investigated whether the degree of GWB was statistically linked to mean intensity and intensity change  
437 rate of the IOP, the height and distance from storm centre of the measurement and the shape of the wind profile at each height level  
438 by compositing 91 observation periods using the results from the WDR fit. Figure 12 summarises the results of the PDF analysis by  
439 showing the probabilities of finding markedly supergradient and subgradient flows in each of the different composites of intensity,  
440 rate of intensification, shape of wind profile, etc. The PDF analysis showed that the composite of periods of stronger storms (Cat. 3, 4  
441 and 5) had a significantly higher likelihood of exhibiting supergradient winds than the composites of weaker storms (TS/TD and Cat.  
442 1-2). These differences were accentuated when observations were composited based on both intensity of the IOP and height of the  
443 measurement as more supergradient winds are found in the upper boundary layer than above.

444 The degree of GWB is less related to the rate of intensification. The distributions of the *weakening*, *intensifying* and *steady-*  
445 *state* composites were not significantly different. Weakening storms show a higher likelihood (Fig. 12) of supergradient winds than  
446 intensifying storms, particularly in the boundary layer. This result seems inconsistent with the implications of the boundary layer spin-  
447 up paradigm (Montgomery *et al.* 2014; Smith and Montgomery 2015; Montgomery and Smith 2017), which argues that supergradient  
448 winds in the boundary layer play an important role for intensification.

449 In contrast, one of the compositing characteristics that led to the largest differences in the PDFs of gradient wind anomalies was the  
450 shape of the wind profile, as separating the wind profiles into *peaked* and *flat* resulted in significantly different PDFs of gradient wind  
451 anomalies. In particular, *peaked* wind profiles had a higher probability of having supergradient winds above  $15 \text{ m s}^{-1}$  than periods  
452 with a *flat* wind profile (Fig. 12). These results agree with the model of Kepert and Wang (2001), in which the radial distribution of  
This article is protected by copyright. All rights reserved.

453 momentum, accounted for as the shape of the wind profile, has a strong relationship to the degree of GWB. *Peaked* wind profiles,  
 454 where the radial gradient of momentum was largest, had a much higher likelihood of presenting supergradient winds than all the other  
 455 composite categories, including the *flat* wind profiles.

456 There are several caveats and factors to consider in this study. For instance, the different composite sizes may affect the PDFs, but  
 457 the statistical tests used account for this factor. Similarly, possible uneven radial distributions of the dropsondes in the observation  
 458 periods could cause biases in several analysed periods. Several criteria were tested to define intensity change categories or the shape of  
 459 the wind profiles and the results did not change depending on the definition.

460 Nevertheless, this is the first study to analyse which characteristics determine GWB in a large number of observation periods.  
 461 Additionally, the comparison between methods suggests that analysis of GWB should use a fitting function that accurately represents  
 462 the wind profile, such as the WDR function, instead of a polynomial function, which may lead to significant artefacts.

### 463 Acknowledgement

464 JLG was supported by a CONACYT-SENER Scholarship (CVU: 701275) and an Oxford-Richards Scholarship. The authors thank  
 465 Will Torgerson for his help with the calculation of the track using the translating fitting pressure method. The authors also thank Jeff  
 466 Kepert for his valuable comments and the discussions on early versions of this manuscript. This and many other studies could not have  
 467 been done without the NOAA, NASA and USAF teams that have been dedicated to deploy dropsondes for over 20 years. The authors  
 468 would also like to thank two anonymous reviewers for their constructive comments that have greatly improved this manuscript.

### 469 Supporting information

- 470 • Figure S1: Gradient wind profile composites based on shape of wind profile criteria.
- 471 • Figure S2: Cumulative density function version of Figure 8.
- 472 • Figure S3: Boxplots version of Figure 8.
- 473 • Figure S4: PDFs as in Figure 8c, showing the sensitivity to the criteria of peaked and flat profiles.

### 474 References

- 475 Abarca SF, Montgomery MT, Braun SA, Dunion J. 2016. On the Secondary Eyewall Formation of Hurricane Edouard (2014). *Monthly Weather Review* **144**:  
 476 3321–3331, doi:10.1175/MWR-D-15-0421.1.
- 477 Bell MM, Montgomery MT. 2008. Observed structure, evolution, and potential intensity of category 5 Hurricane Isabel (2003) from 12 to 14 September. *Monthly*  
 478 *Weather Review* **136**: 2023–2046.
- 479 Bell MM, Montgomery MT, Lee WC. 2012. An axisymmetric view of concentric eyewall evolution in Hurricane Rita (2005). *Journal of the Atmospheric*  
 480 *Sciences* **69**: 2414–2432.
- 481 Braun SA, Kakar R, Zipser E, Heymsfield G, Albers C, Brown S, Durden SL, Guimond S, Halverson J, Heymsfield A, Ismail S, Lambrigtsen B, Miller T, Tanelli  
 482 S, Thomas J, Zawislak J. 2013. NASA's Genesis and Rapid Intensification Processes (GRIP) field experiment. *Bulletin of the American Meteorological Society*  
 483 **94**: 345–363.
- 484 Bui HH, Smith RK, Montgomery MT, Peng J. 2009. Balanced and unbalanced aspects of tropical cyclone intensification. *Quarterly Journal of the Royal*  
 485 *Meteorological Society* **135**: 1715–1731.
- 486 Cione JJ, Kalina EA, Zhang JA, Uhlhorn EW. 2013. Observations of air-sea interaction and intensity change in hurricanes. *Monthly Weather Review* **141**:  
 487 2368–2382.
- 488 Didlake AC, Houze RA. 2011. Kinematics of the secondary eyewall observed in Hurricane Rita (2005). *Journal of the Atmospheric Sciences* **68**: 1620–1636.
- 489 Emanuel KA. 1997. Some aspects of hurricane inner-core dynamics and energetics. *Journal of the Atmospheric Sciences* **54**: 1014–1026.
- 490 Franklin JL, Black ML, Valde K. 2003. GPS dropwindsonde wind profiles in hurricanes and their operational implications. *Weather and Forecasting* **18**: 32–44.
- 491 Gray WM. 1962. On the balance of forces and radial accelerations in hurricanes. *Quarterly Journal of the Royal Meteorological Society* **88**: 430–458.
- 492 Gray WM. 1991. Comments on gradient balance in tropical cyclones. *Journal of the Atmospheric Sciences* **48**: 1201–1208.

- 493 Gray WM, Shea DJ. 1973. The hurricanes inner core region. Part II: Thermal stability and dynamic characteristics. *Journal of the Atmospheric Sciences* **30**:  
494 1565–1576.
- 495 Hendricks EA, Peng MS, Fu B, Li T. 2010. Quantifying environmental control on tropical cyclone intensity change. *Monthly Weather Review* **138**: 3243–3271.
- 496 Heng J, Wang Y, Zhou W. 2017. Revisiting the balanced and unbalanced aspects of tropical cyclone intensification. *Journal of the Atmospheric Sciences* **74**:  
497 2575–2591.
- 498 Holland GJ. 1980. An analytic model of the wind and pressure profiles in hurricanes. *Monthly weather review* **108**: 1212–1218.
- 499 Holton JR, Hakim GJ. 2012. *An introduction to dynamic meteorology, International Geophysics Series*, vol. 88. Academic press, 4 edn.
- 500 Jorgensen DP. 1984. Mesoscale and Convective-Scale Characteristics of Mature Hurricanes. Part II. Inner Core Structure of Hurricane Allen (1980). *Journal of*  
501 *the Atmospheric Sciences* **41**: 1287–1311.
- 502 Judt F, Chen SS. 2010. Convectively generated potential vorticity in rainbands and formation of the secondary eyewall in Hurricane Rita of 2005. *Journal of the*  
503 *Atmospheric Sciences* **67**: 3581–3599.
- 504 Kepert JD. 2001. The dynamics of boundary layer jets within the tropical cyclone core. Part I: Linear theory. *Journal of the Atmospheric Sciences* **58**: 2469–2484.
- 505 Kepert JD. 2005. Objective analysis of tropical cyclone location and motion from high-density observations. *Monthly Weather Review* **133**: 2406–2421.
- 506 Kepert JD. 2006a. Observed boundary layer wind structure and balance in the hurricane core. Part I: Hurricane Georges. *Journal of the Atmospheric Sciences*  
507 **63**: 2169–2193.
- 508 Kepert JD. 2006b. Observed boundary layer wind structure and balance in the hurricane core. Part II: Hurricane Mitch. *Journal of the Atmospheric Sciences* **63**:  
509 2194–2211.
- 510 Kepert JD, Wang Y. 2001. The dynamics of boundary layer jets within the tropical cyclone core. Part II: Nonlinear enhancement. *Journal of the Atmospheric*  
511 *Sciences* **58**: 2485–2501.
- 512 Landsea CW, Franklin JL. 2013. Atlantic hurricane database uncertainty and presentation of a new database format. *Monthly Weather Review* **141**: 3576–3592.
- 513 Miyamoto Y, Satoh M, Tomita H, Oouchi K, Yamada Y, Kodama C, Kinter James I. 2014. Gradient Wind Balance in Tropical Cyclones in High-Resolution  
514 Global Experiments. *Monthly Weather Review* **142**(5): 1908–1926, doi:10.1175/MWR-D-13-00115.1.
- 515 Montgomery MT, Bell MM, Abernethy SD, Black ML. 2006. Hurricane Isabel (2003): New insights into the physics of intense storms. Part I: Mean vortex  
516 structure and maximum intensity estimates. *Bulletin of the American Meteorological Society* **87**: 1335–1348.
- 517 Montgomery MT, Smith RK. 2017. Recent developments in the fluid dynamics of tropical cyclones. *Annual Review of Fluid Mechanics* **49**: 541–574.
- 518 Montgomery MT, Zhang JA, Smith RK. 2014. An analysis of the observed low level structure of rapidly intensifying and mature hurricane Earl (2010). *Quarterly*  
519 *Journal of the Royal Meteorological Society* **140**: 2132–2146.
- 520 Penland AG, Willoughby HE. 2009. Diabatically induced secondary flows in tropical cyclones. Part I: Quasi-steady forcing. *Monthly Weather Review* **137**:  
521 805–821.
- 522 Rogers RF, Reasor PD, Lorsolo S. 2013. Airborne doppler observations of the inner-core structural differences between intensifying and steady-state tropical  
523 cyclones. *Monthly Weather Review* **141**: 2970–2991.
- 524 Rogers RF, Reasor PD, Zhang JA. 2015. Multiscale structure and evolution of hurricane earl (2010) during rapid intensification. *Monthly Weather Review* **143**:  
525 536–562.
- 526 Rogers RF, Uhlhorn E. 2008. Observations of the structure and evolution of surface and flight-level wind asymmetries in Hurricane Rita (2005). *Geophysical*  
527 *Research Letters* **35**, doi:10.1029/2008GL034774.
- 528 Sanger NT, Montgomery MT, Smith RK, Bell MM. 2014. An observational study of tropical cyclone spinup in Supertyphoon Jangmi (2008) from 24 to 27  
529 September. *Monthly Weather Review* **142**: 3–28.
- 530 Schwendike J, Kepert JD. 2008. The boundary layer winds in Hurricanes Danielle (1998) and Isabel (2003). *Monthly Weather Review* **136**: 3168–3192.
- 531 Shapiro LJ, Willoughby HE. 1982. The response of balanced hurricanes to local sources of heat and momentum. *Journal of the Atmospheric Sciences* **39**:  
532 378–394.
- 533 Smith RK, Montgomery MT. 2010. Hurricane boundary-layer theory. *Quarterly Journal of the Royal Meteorological Society* **136**: 1665–1670.
- 534 Smith RK, Montgomery MT. 2015. Toward Clarity on Understanding Tropical Cyclone Intensification. *Journal of the Atmospheric Sciences* **72**: 3020–3031.
- 535 Smith RK, Montgomery MT. 2016. Understanding hurricanes. *Weather* **71**: 219–223.
- 536 Stern DP, Kepert JD, Bryan GH, Doyle JD. 2020. Understanding atypical midlevel wind speed maxima in hurricane eyewalls. *Journal of the Atmospheric*  
537 *Sciences* **77**: 1531–1557.

- 538 Vigh J, *et al.* 2015. FLIGHT+: The extended flight level dataset for tropical cyclones. *Tropical Cyclone Data Project, National Center for Atmospheric Research,*  
539 *Research Applications Laboratory, Boulder, Colorado.* [Available online at: [http://dx. doi. org/10. 5065/D6WS8R93](http://dx.doi.org/10.5065/D6WS8R93)] Accessed: March 25th, 2018.
- 540 Wang JJ, Young K, Hock T, Lauritsen D, Behringer D, Black M, Black PG, Franklin J, Halverson J, Molinari J, Nguyen L, Reale T, Smith J, Sun B, Wang  
541 Q, Zhang JA. 2015. A long-term, high-quality, high-vertical-resolution gps dropsonde dataset for hurricane and other studies. *Bulletin of the American*  
542 *Meteorological Society* **96**: 961–973.
- 543 Willoughby H. 1979. Forced secondary circulations in hurricanes. *Journal of Geophysical Research: Oceans* **84**: 3173–3183.
- 544 Willoughby HE. 1990. Gradient balance in tropical cyclonesff. *Journal of the Atmospheric Sciences* **47**: 265–274.
- 545 Willoughby HE, Clos JA, Shoreibah MG. 1982. Concentric eye walls, secondary wind maxima, and the evolution of the hurricane vortex. *Journal of the*  
546 *Atmospheric Sciences* **39**: 395–411.
- 547 Willoughby HE, Darling RWR, Rahn ME. 2006. Parametric representation of the primary hurricane vortex. Part II: A new family of sectionally continuous  
548 profiles. *Monthly Weather Review* **134**: 1102–1120.
- 549 Zhang JA, Rogers RF, Nolan DS, Jr FDM. 2011. On the characteristic height scales of the hurricane boundary layer. *Monthly Weather Review* **139**: 2523–2535.
- 550 Zhang JA, Rogers RF, Reasor PD, Uhlhorn EW, Marks Jr FD. 2013. Asymmetric hurricane boundary layer structure from dropsonde composites in relation to  
551 the environmental vertical wind shear. *Monthly Weather Review* **141**: 3968–3984.

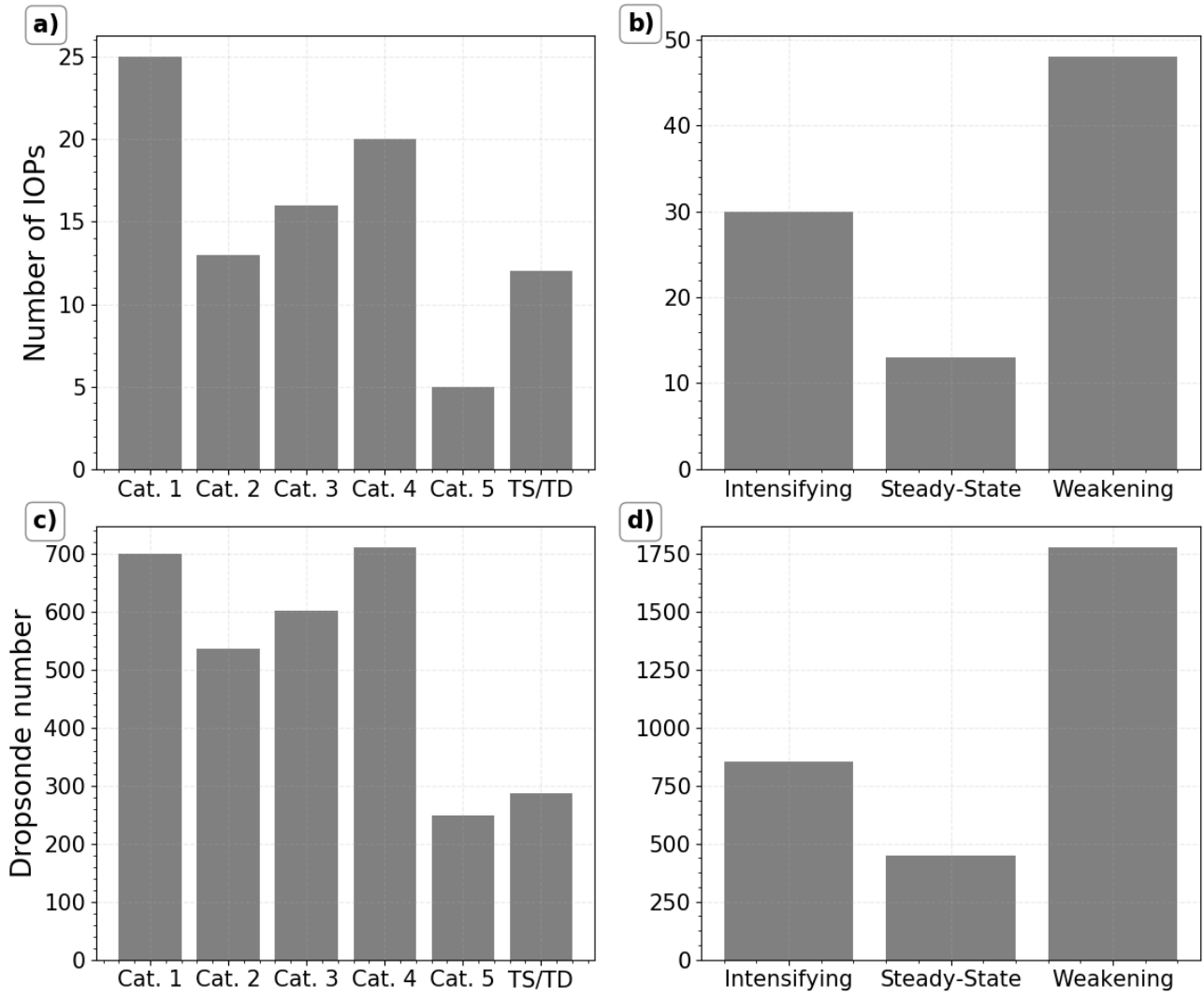
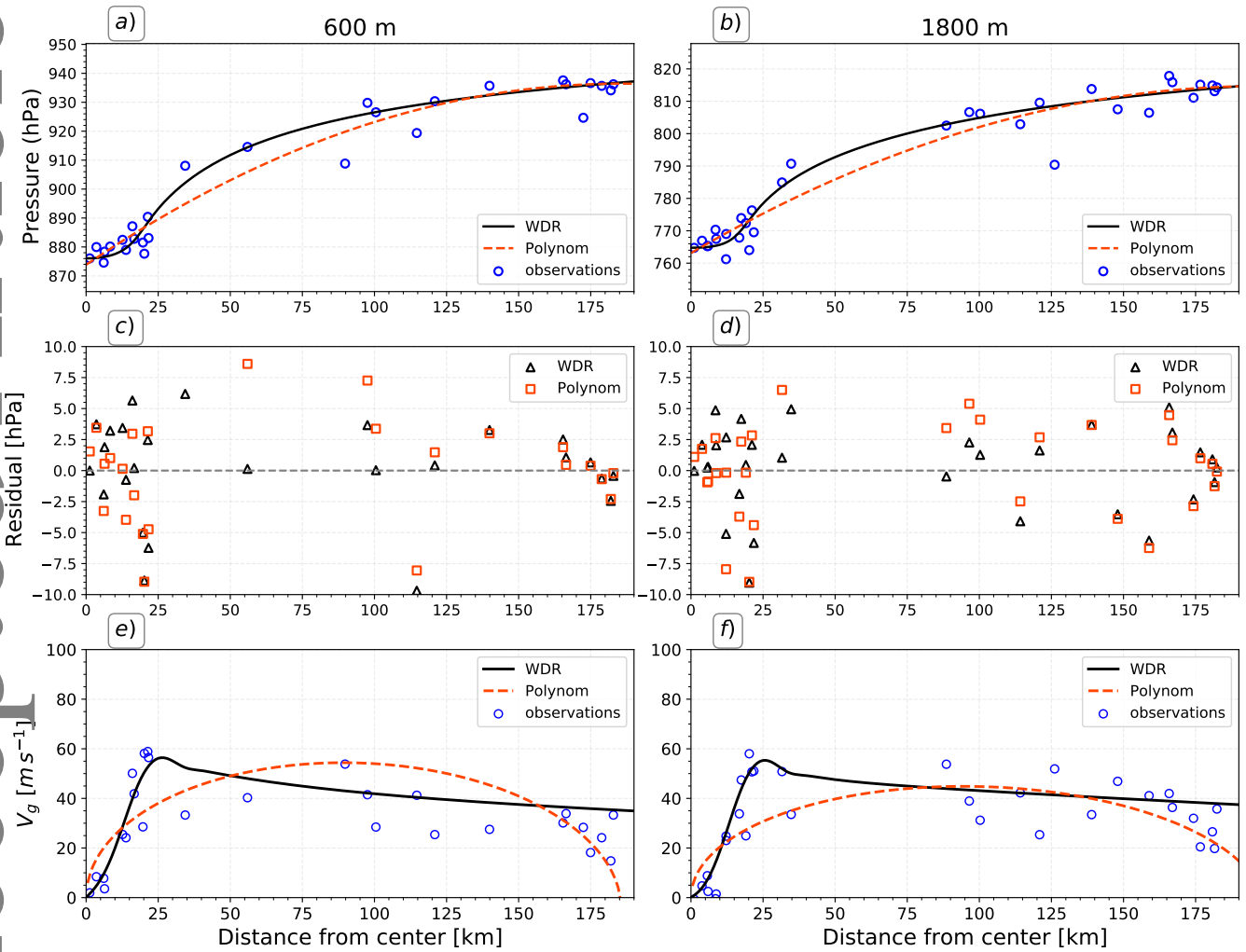


Figure 1. (a, b) Number of IOPs and (c, d) total dropsonde number for each of the (a, c) intensity and (b, d) intensity change categories. The total dropsonde number includes only dropsondes within a 220-km radius from the storm centre.



**Figure 2.** Gradient wind balance assessment during 18 UTC on 30 August to 00 UTC on 31 August 2010 (IOP 72 in Table 1) of Hurricane Earl (2010). (a, b) show the pressure observations (circles) with the polynomial (dashed red) and WDR (solid black) pressure fits. (c, d) show the residuals from the fits, in units of hPa. (e, f) The gradient wind profiles ( $V_g$ ) from each fitting method is shown, as well as the observed tangential wind (circles). Results are shown at (a, c, e) 600 m and (b, d, f) 1800 m height.

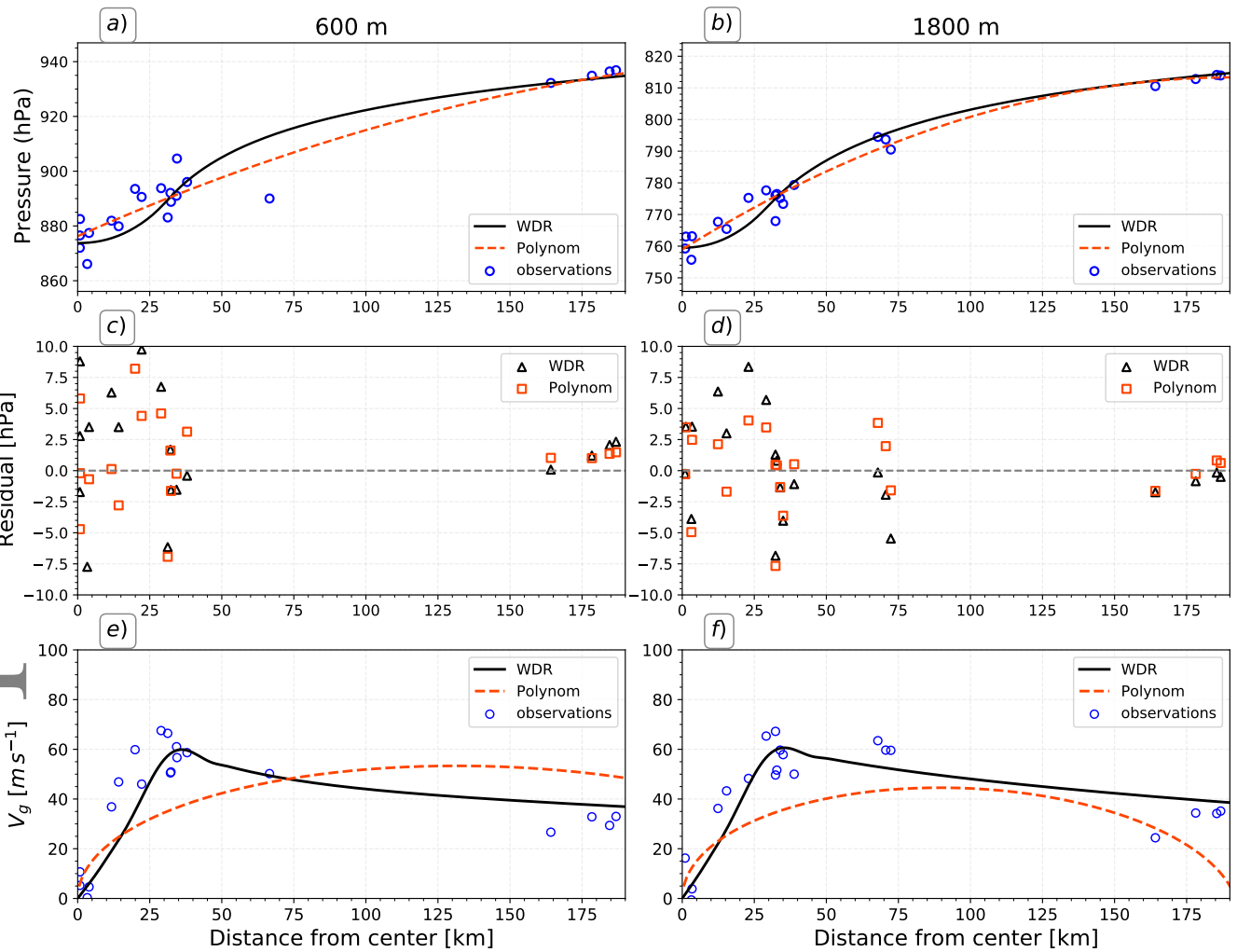


Figure 3. As in Figure 2, but for 06-18 UTC on 2 September 2010 (IOP 75 in Table 1) of Hurricane Earl (2010).

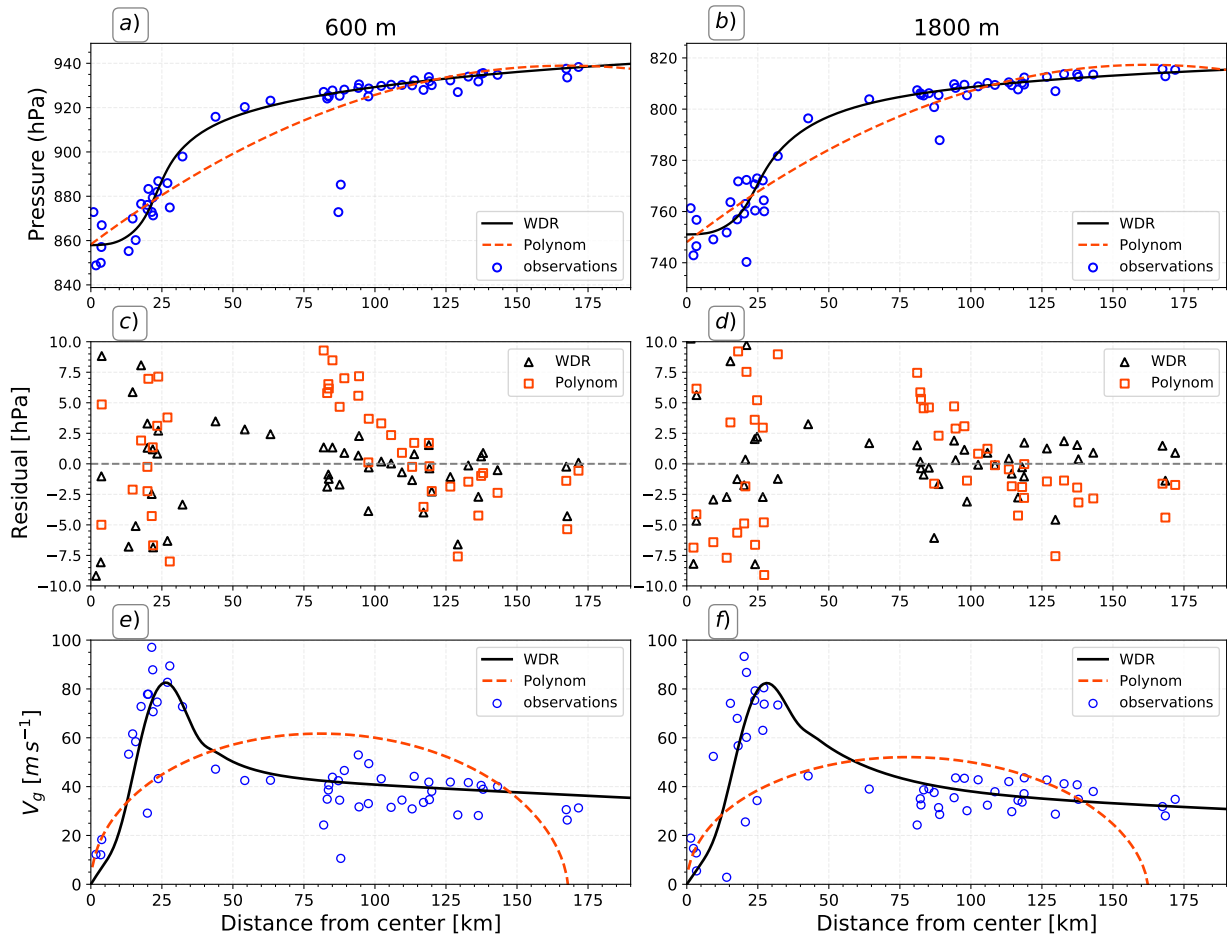
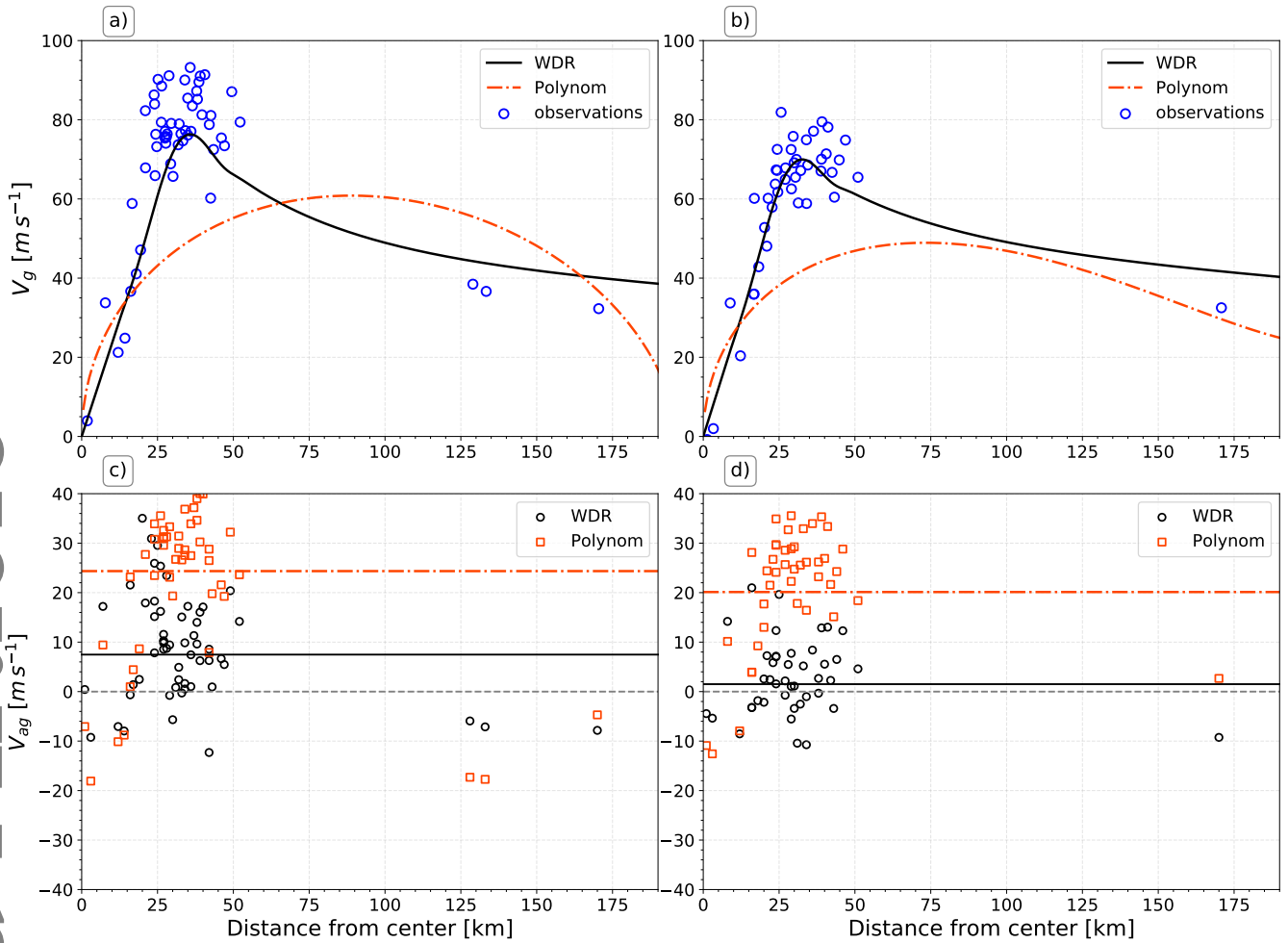
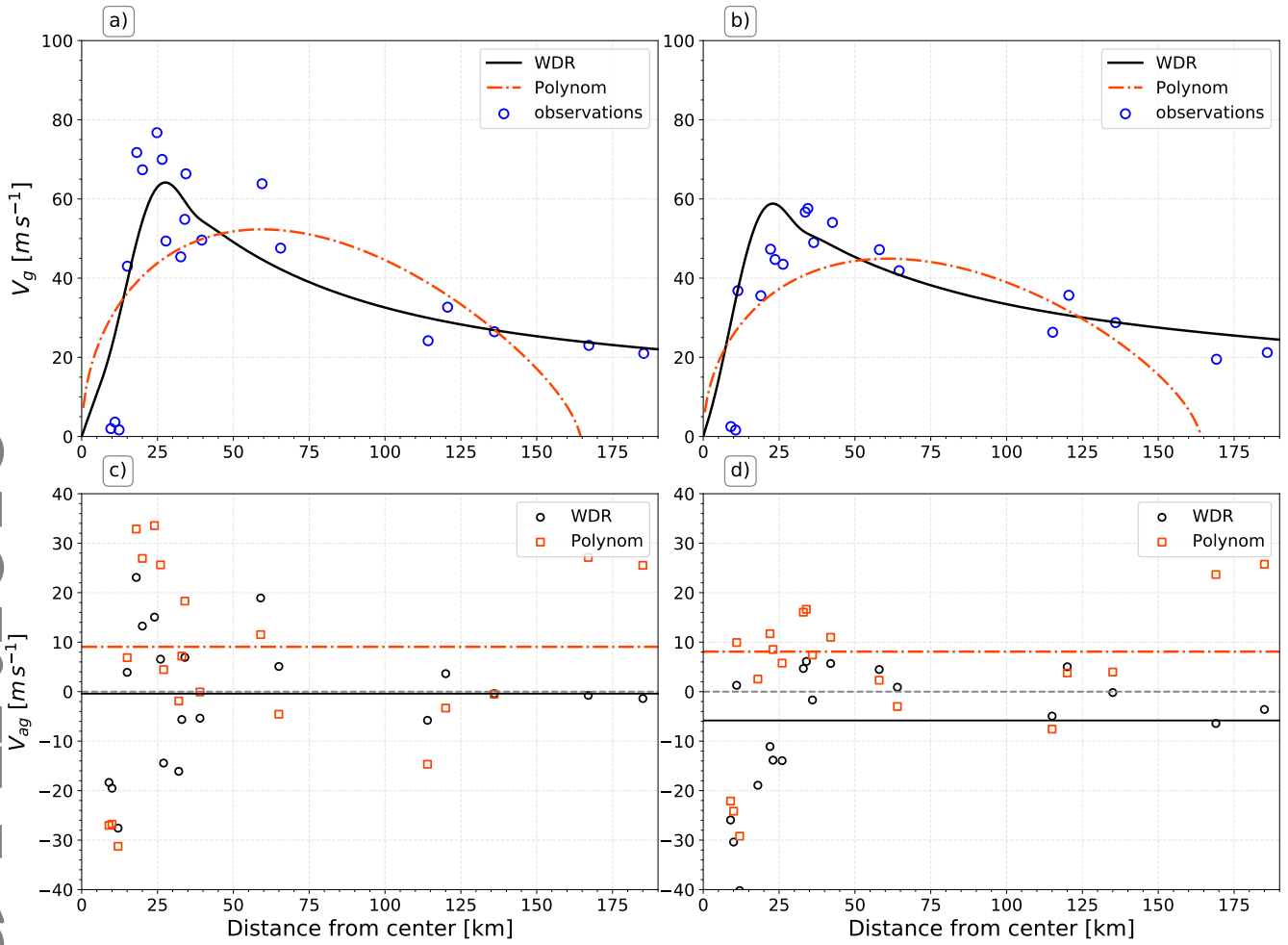


Figure 4. As in Figure 2, but for 15-21 UTC on 21 September, 2005 (IOP 44 in Table 1) of Hurricane Rita (2005).



**Figure 5.** (a, b) Tangential wind observations (blue circles) and estimated gradient winds ( $V_g$ ) from the polynomial (red) and the WDR functions (black) for Hurricane IOP 20 for 16-21 UTC on 12 September 2005 (IOP 20 from Table 1) is shown. (c, d) The gradient wind ( $V_{ag}$ ), a measure of the degree of GWB, is shown for each wind observation. The black (red) dashed line illustrates the mean  $V_{ag}$  for the WDR (polynomial) fit. Results are shown at the (a, c) 600-m level and (b, d) the 1800-m level.



**Figure 6.** As in Figure 5, but for Hurricane Michelle from 18 UTC 3 November to 05 UTC 4 November (2001) (IOP 13 in Table 1).

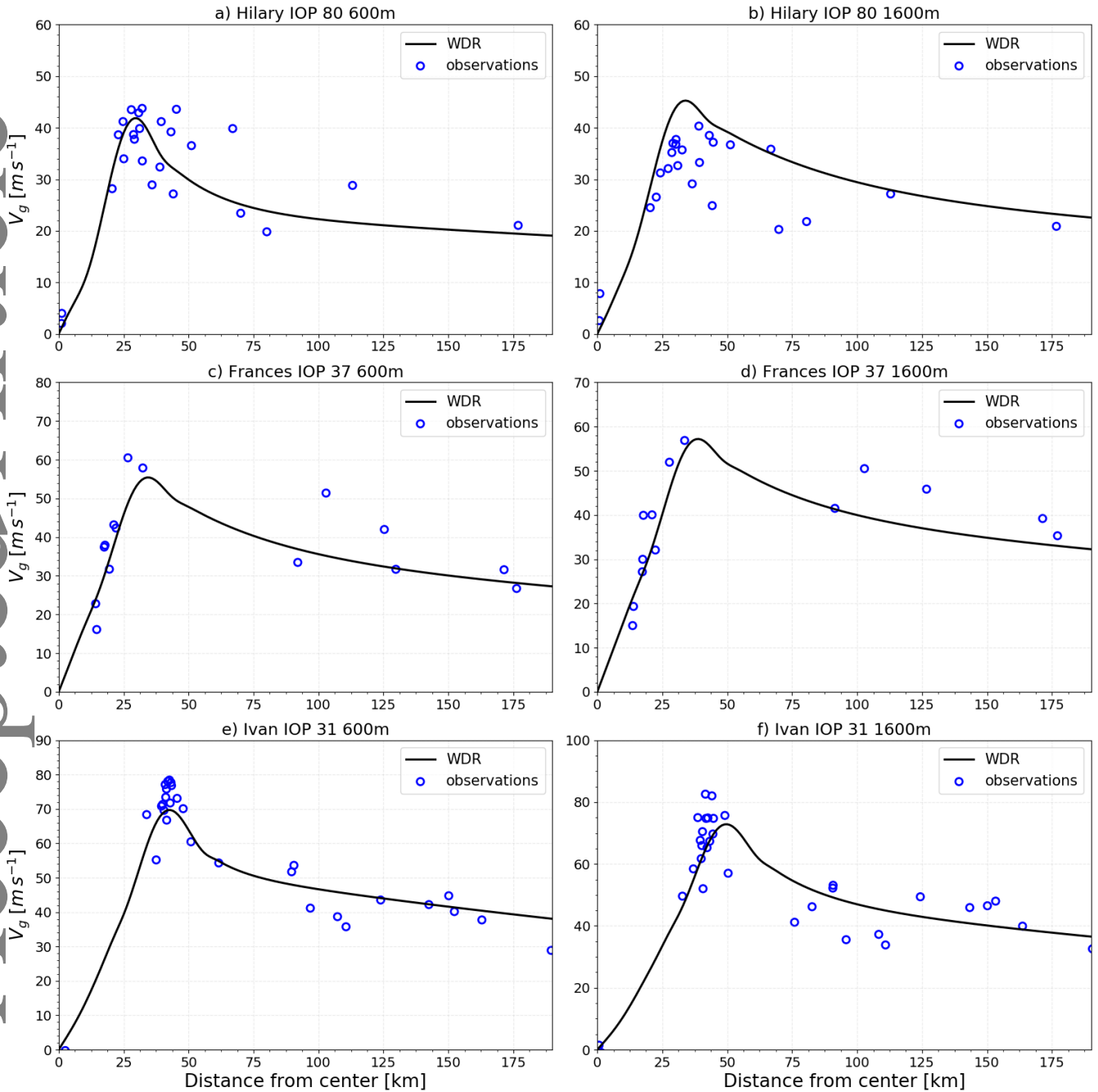


**Figure 7.** Gradient wind from the WDR function (black) and dropsonde observations (blue circles) for IOPs of Hurricanes (a, b) Hilary (2011), (c, d) Frances (2004), and (e, f) Ivan (2004). Panels (a,c,e) represent the top of the boundary layer (600 m) whereas (b, d, f) are above the inflow layer (1600 m).

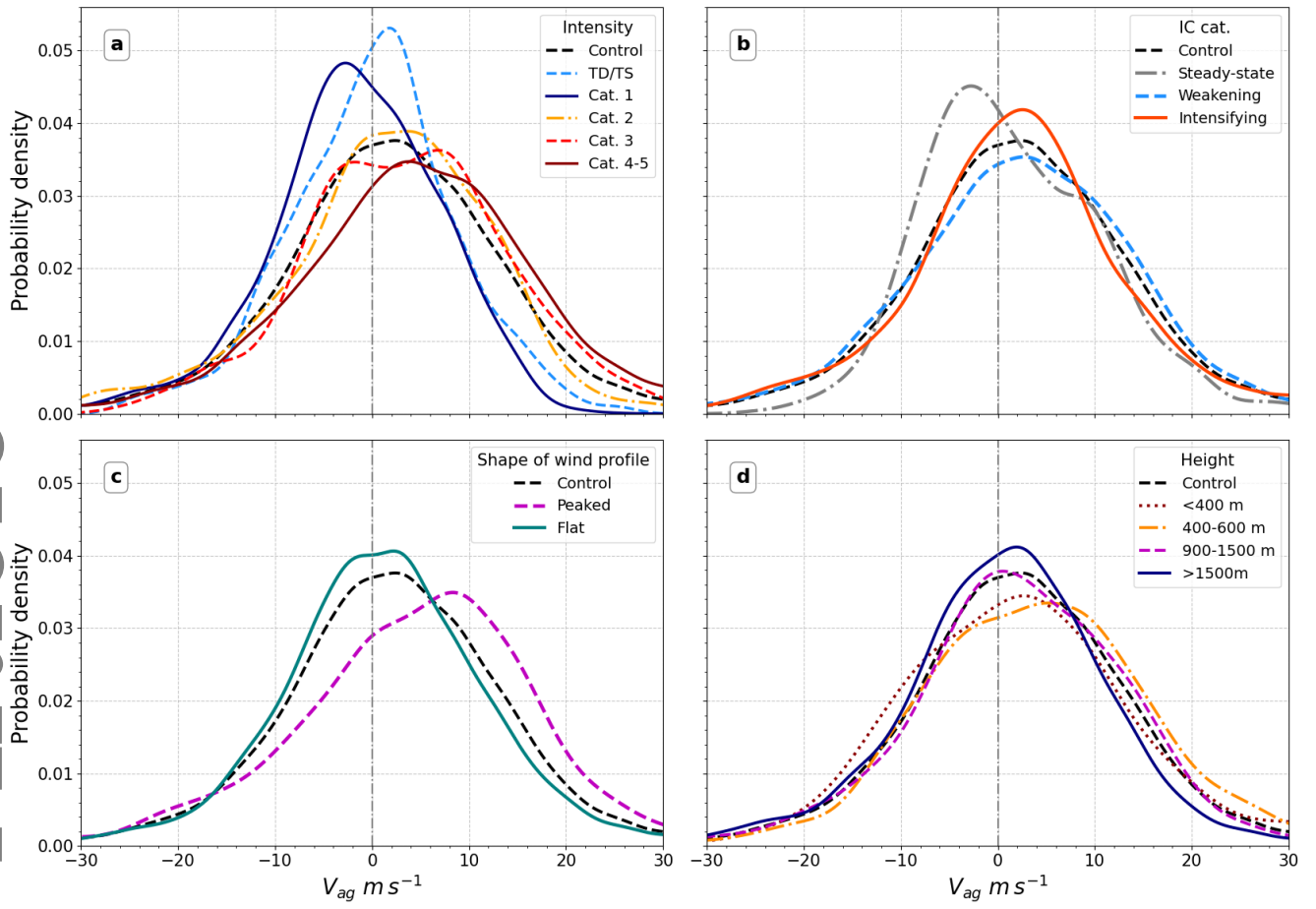


**Figure 8.** Probability density functions of the  $V_{ag}$  ( $m s^{-1}$ ) of all IOPs in the inner-core ( $RMW/2 < r < 3RMW/2$ ) composed by (a) the mean intensity, (b) the intensity change category, (c) the shape of the wind profile and (d) four height intervals. The *Control* (dashed black line) PDF is the distribution of the sample of the  $V_{ag}$  from all IOPs at all heights, also in the inner-core.

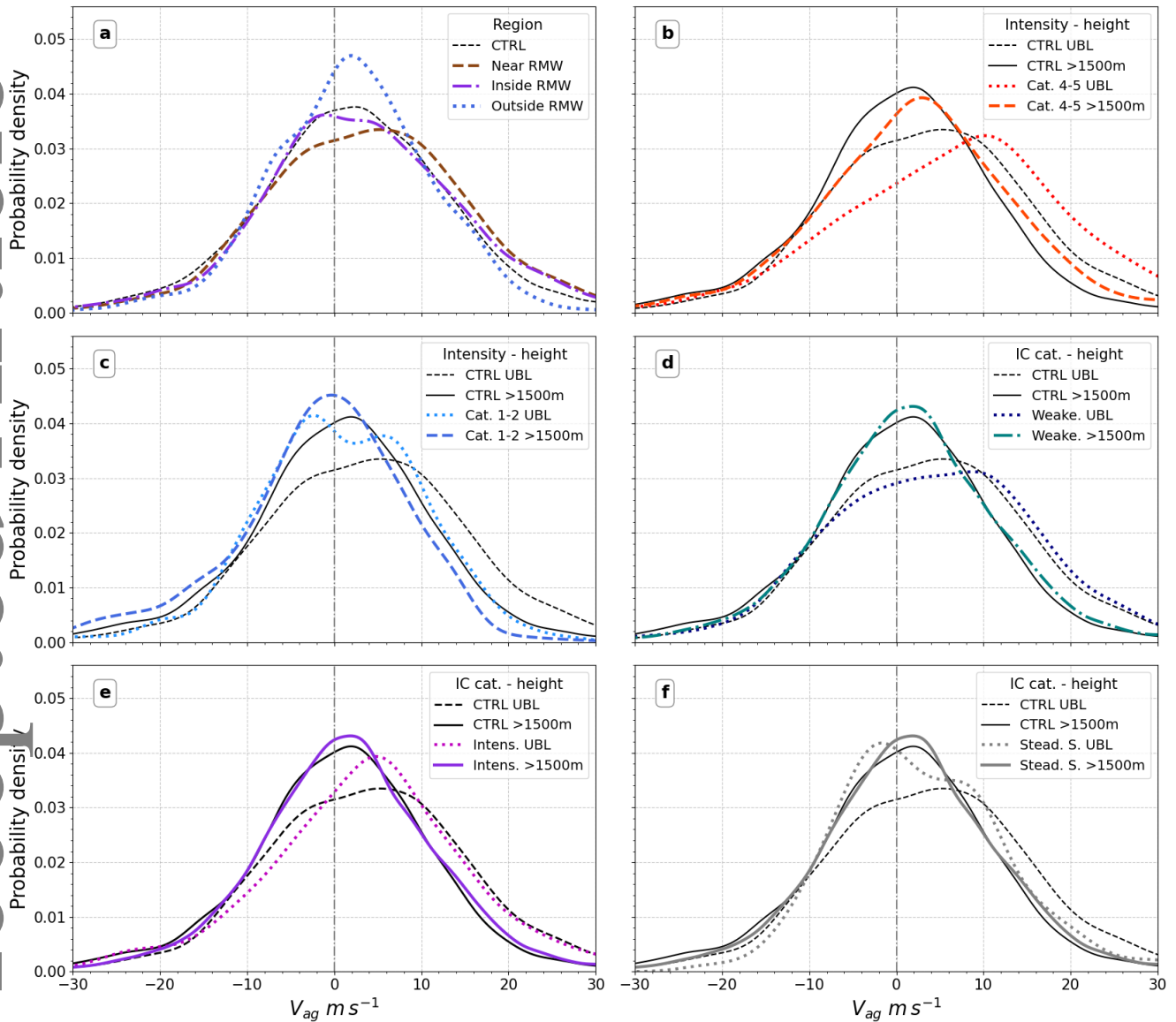


**Figure 9.** PDFs as in Figure 8. (a) shows the effect of the radial distance to storm centre by compositing for observations near the RMW ( $RMW/2 < r < 3RMW/2$ ), inside the RMW ( $0 < r < RMW/2$ ), and outside the RMW ( $r > 3RMW/2$ ). These PDFs, as well as the *Control* in this panel only contain observations in the interval of 400-600 m, the upper boundary layer (UBL). (b) PDFs of inner-core observations in Cat. 4-5 IOPs in the UBL (400-600 m) and the observations above 1500 m. (c) is as in (b) but for Cat. 1-2 IOPs. (d, e, f) as in (b) but for Intensity change (IC) categories: weakening, intensifying and steady-state storms. The *Control* was also subsampled at these two height intervals in (b-f).

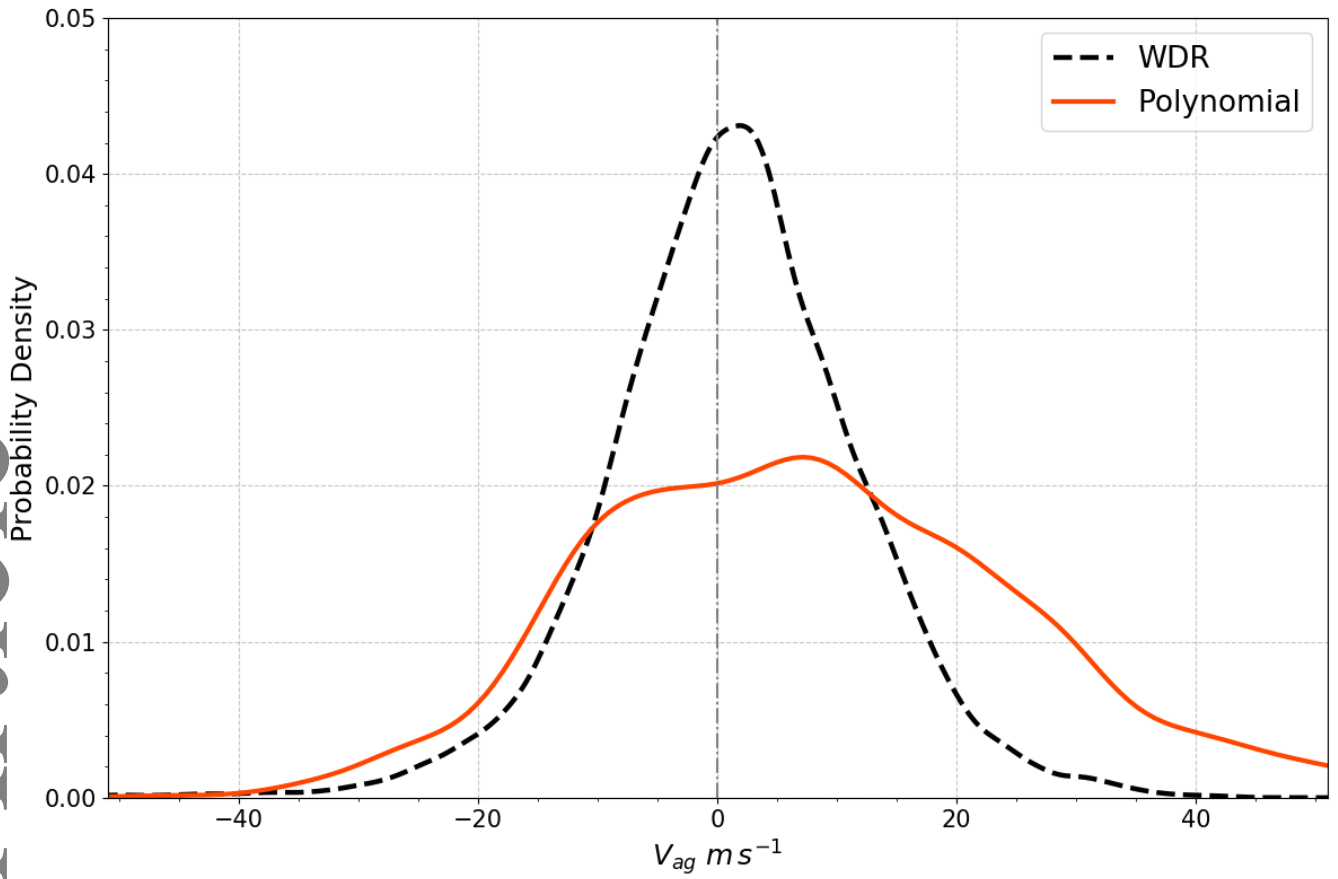


**Figure 10.** PDFs of gradient wind anomalies  $V_{ag}$  computed from the WDR function (black dashed line) and the polynomial fit (orange solid line) at all height levels for all IOPs. The WDR function PDF is the same as the *Control* in the previous figures (e.g. Figure 8).

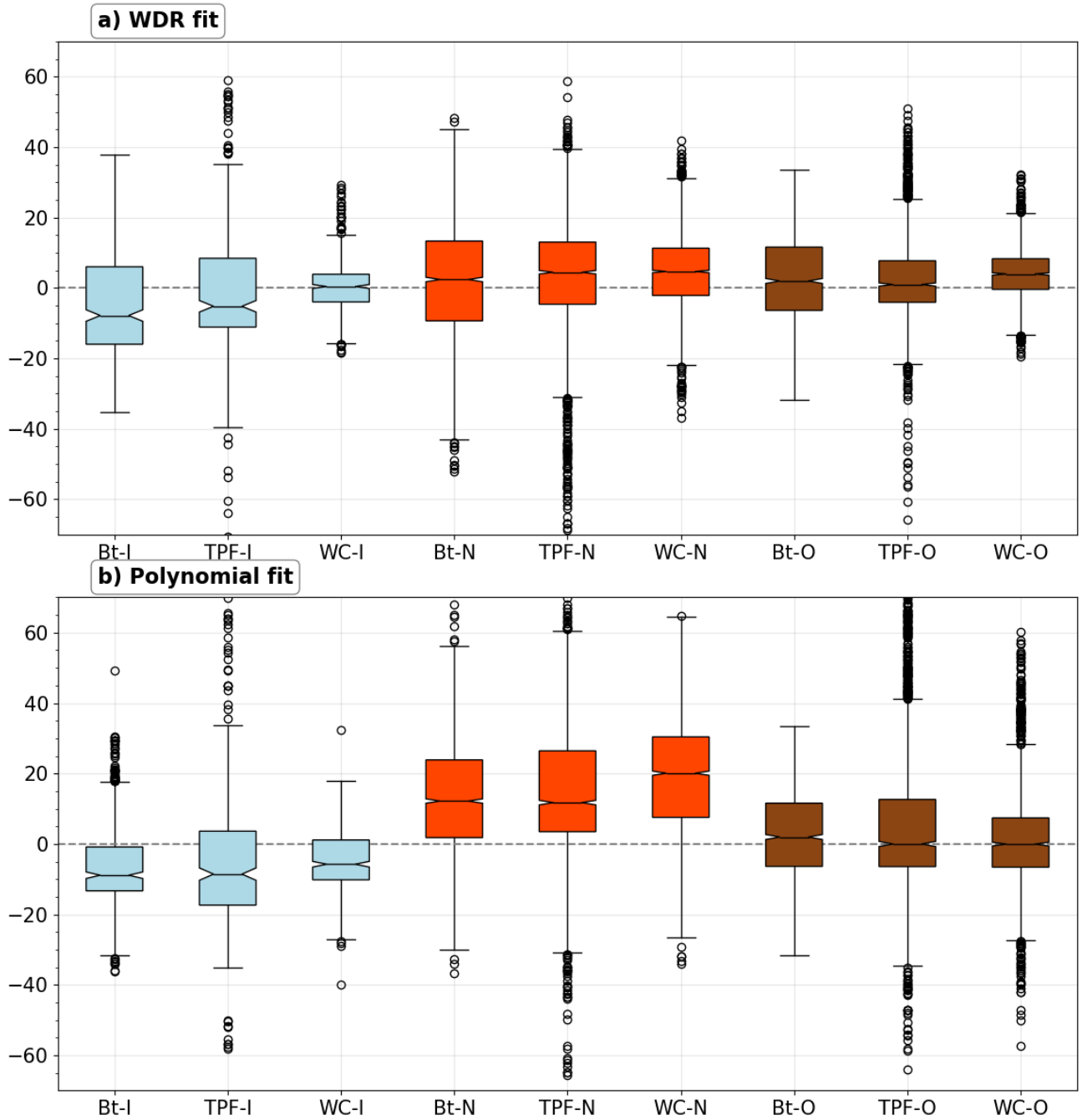


**Figure 11.** Boxplots of gradient wind balance anomalies ( $V_{ag}$ ) computed using the best-track (BT), the translating pressure fit (TPF) and the Willoughby-Chelmw (WC) track finding algorithms in three different radial regions: inside (I, blue), near (N, red) and outside (O, maroon) the RMW. The boxplots are shown using (a) the WDR function and (b) the polynomial fit.

More likely subgradient →

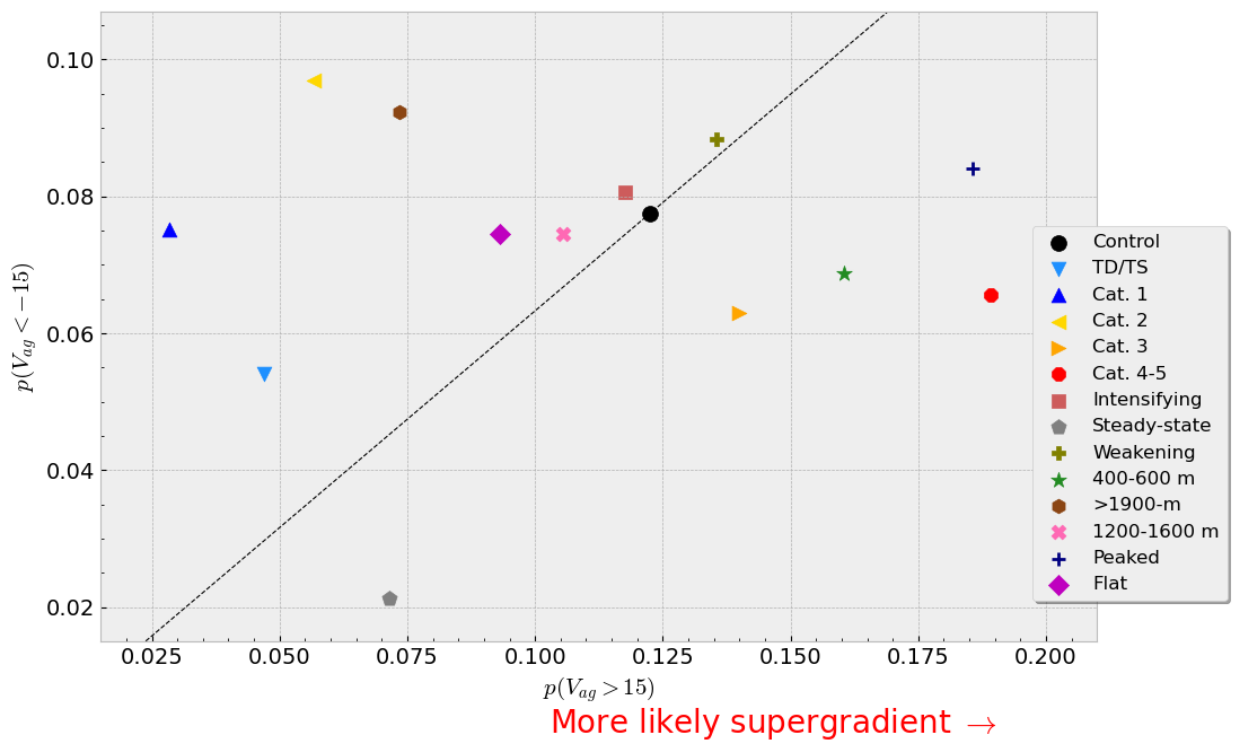


**Figure 12.** Scatter plot of the probabilities of  $V_{ag}$  being markedly supergradient ( $p(V_{ag} > 15)$ ) versus being strongly subgradient ( $p(V_{ag} < -15)$ ). These probabilities were estimated for observations in the inner-core ( $RMW/2 < r < 3RMW/2$ ) that were then separated into categories of intensity, rate of intensification, shape of the wind profile and height. The black dot (Control) includes all the  $V_{ag}$  estimations in the inner-core and the dashed line follows the same proportion of supergradient likelihood to subgradient likelihood as the Control.

Table 1. Information on the intense-observation periods (IOPs) used in this study. The table reports the start and end dates, the mean intensity  $\bar{I}$  ( $kt$ ), the intensity category (I. Cat.), the intensity change rate ( $ICR$  ;  $kt$  ( $24$  h) $^{-1}$ ), the number of dropsondes in the inner-core (Drops), and whether the shape of the wind profile (WPS) was found to be peaked (P) or flat/non-peaked (NP) in (BL) or above (ABL) the boundary layer.

IOP	Storm	Start date hour	End date hour	$\bar{I}$ (kt)	I. Cat.	ICR ( $kt/24$ -h)	Drops	WPS	
								BL	ABL
1	Irene	1999-10-15 20	1999-10-16 01	65.0	Cat. 1	-10.0	25	NP	NP
2	Bret	1999-08-21 17	1999-08-21 21	105.0	Cat. 3	70.0	13	P	NP
3	Bret	1999-08-21 21	1999-08-22 03	105.0	Cat. 3	10.0	12	P	NP
4	Floyd	1999-09-12 18	1999-09-13 02	125.0	Cat. 4	20.0	19	P	NP
5	Floyd	1999-09-13 17	1999-09-14 01	120.0	Cat. 4	-20.0	36	NP	NP
6	Floyd	1999-09-15 20	1999-09-16 09	90.0	Cat. 2	-40.0	62	NP	NP
7	Dennis	1999-08-26 18	1999-08-26 21	65.0	Cat. 1	-10.0	15	NP	NP
8	Dennis	1999-08-26 21	1999-08-27 02	65.0	Cat. 1	0.0	3	NP	NP
9	Dennis	1999-08-29 18	1999-08-30 01	90.0	Cat. 2	-10.0	25	NP	NP
10	Gabrielle	2001-09-15 17	2001-09-16 00	47.5	TS/TD	10.0	35	NP	NP
11	Humberto	2001-09-23 19	2001-09-24 02	85.0	Cat. 2	-30.0	69	NP	NP
12	Humberto	2001-09-24 18	2001-09-25 00	65.0	Cat. 1	0.0	77	NP	NP
13	Michelle	2001-11-03 18	2001-11-04 05	115.0	Cat. 4	10.0	31	P	P
14	Michelle	2001-11-04 11	2001-11-04 17	120.0	Cat. 4	-30.0	14	P	NP
15	Lili	2002-09-30 18	2002-10-01 01	70.0	Cat. 1	40.0	34	NP	NP
16	Lili	2002-10-02 02	2002-10-02 11	100.0	Cat. 3	45.0	39	P	P
17	Lili	2002-10-02 17	2002-10-03 01	123.3	Cat. 4	-90.0	46	P	P
18	Isidore	2002-09-21 18	2002-09-22 00	110.0	Cat. 3	0.0	73	P	NP
19	Isidore	2002-09-22 18	2002-09-23 01	105.0	Cat. 3	-100.0	27	NP	NP
20	Isabel	2003-09-12 16	2003-09-12 21	140.0	Cat. 5	-20.0	77	P	NP
21	Isabel	2003-09-13 16	2003-09-14 01	137.5	Cat. 5	-10.0	43	NP	NP
22	Isabel	2003-09-14 16	2003-09-15 00	135.0	Cat. 4	-30.0	76	NP	NP
23	Isabel	2003-09-18 14	2003-09-18 19	87.5	Cat. 2	-80.0	30	NP	P
24	Fabian	2003-09-02 17	2003-09-02 23	120.0	Cat. 4	-20.0	65	NP	NP
25	Fabian	2003-09-03 17	2003-09-03 22	110.0	Cat. 3	-10.0	59	NP	NP
26	Jeanne	2004-09-24 17	2004-09-25 00	85.0	Cat. 2	10.0	30	NP	NP
27	Jeanne	2004-09-25 18	2004-09-26 02	105.0	Cat. 3	-60.0	53	NP	NP
28	Ivan	2004-09-09 16	2004-09-10 00	130.0	Cat. 4	-10.0	26	P	P
29	Ivan	2004-09-12 06	2004-09-13 00	133.7	Cat. 4	20.0	47	P	P
30	Ivan	2004-09-13 18	2004-09-14 00	140.0	Cat. 5	-30.0	34	P	P
31	Ivan	2004-09-14 06	2004-09-15 00	121.6	Cat. 4	0.0	50	P	P
32	Ivan	2004-09-15 00	2004-09-15 12	117.5	Cat. 4	-10.0	21	NP	NP
33	Ivan	2004-09-15 17	2004-09-16 05	112.5	Cat. 3	-80.0	68	NP	NP
34	Frances	2004-08-30 17	2004-08-31 00	110.0	Cat. 3	20.0	21	P	P
35	Frances	2004-08-31 16	2004-08-31 19	125.0	Cat. 4	-10.0	17	NP	NP

36	Frances	2004-09-01 16	2004-09-02 00	120.0	Cat. 4	10.0	39	P	P
37	Frances	2004-09-02 17	2004-09-03 00	110.0	Cat. 3	-30.0	25	NP	NP
38	Frances	2004-09-03 15	2004-09-03 23	90.0	Cat. 2	-5.0	28	P	P
39	Ophelia	2005-09-09 12	2005-09-09 18	62.5	TS/TD	-10.0	25	P	P
40	Ophelia	2005-09-11 11	2005-09-12 01	65.0	Cat. 1	-10.0	50	NP	NP
41	Rita	2005-09-19 16	2005-09-19 21	60.0	TS/TD	0.0	30	NP	NP
42	Rita	2005-09-19 21	2005-09-20 05	60.0	TS/TD	20.0	15	NP	NP
43	Rita	2005-09-20 14	2005-09-21 03	90.	Cat. 2	50.0	26	NP	NP
44	Rita	2005-09-21 15	2005-09-21 20	147.5	Cat. 5	20.0	65	P	P
45	Rita	2005-09-21 20	2005-09-22 13	150.0	Cat. 5	-60.0	13	P	NP
46	Rita	2005-09-22 13	2005-09-22 22	95.0	Cat. 2	-20.0	99	P	NP
47	Rita	2005-09-22 22	2005-09-23 13	147.5	Cat. 5	-10.0	29	P	P
48	Rita	2005-09-23 13	2005-09-23 20	128.3	Cat. 4	-20.0	74	NP	NP
49	Rita	2005-09-23 20	2005-09-24 08	113.3	Cat. 3	-80.0	80	P	NP
50	Ophelia	2005-09-14 14	2005-09-15 00	75.0	Cat. 1	-10.0	16	NP	NP
51	Dennis	2005-07-07 18	2005-07-08 07	116.6	Cat. 4	20.0	15	NP	NP
52	Dennis	2005-07-09 06	2005-07-09 13	80.0	Cat. 1	60.0	17	NP	NP
53	Katrina	2005-08-27 14	2005-08-28 01	100.0	Cat. 3	50.0	46	NP	NP
54	Katrina	2005-08-28 17	2005-08-29 11	131.2	Cat. 4	-65.0	60	P	P
55	Ernesto	2006-08-31 13	2006-08-31 19	60.0	TS/TD	-10.0	22	NP	NP
56	Helene	2006-09-17 14	2006-09-17 18	90.0	Cat. 2	30.0	16	NP	P
57	Helene	2006-09-19 16	2006-09-19 20	90.0	Cat. 2	0.0	20	NP	NP
58	Dolly	2008-07-22 08	2008-07-22 14	55.0	TS/TD	20.0	20	NP	NP
59	Dolly	2008-07-22 23	2008-07-23 02	65.0	Cat. 1	40.0	18	NP	NP
60	Gustav	2008-08-31 06	2008-09-01 01	96.6	Cat. 2	0.0	45	NP	NP
61	Gustav	2008-09-01 01	2008-09-01 19	91.25	Cat. 2	-70.0	51	NP	NP
62	Ike	2008-09-06 14	2008-09-07 00	115.0	Cat. 4	0.0	21	P	P
63	Ike	2008-09-07 17	2008-09-08 00	110.0	Cat. 3	-60.0	18	P	NP
64	Ike	2008-09-09 19	2008-09-10 10	75.0	Cat. 1	30.0	22	NP	NP
65	Ike	2008-09-10 18	2008-09-11 12	85.0	Cat. 2	0.0	27	NP	NP
66	Paloma	2008-11-08 14	2008-11-08 18	125.0	Cat. 4	-140.0	13	P	P
67	Earl	2010-08-28 18	2010-08-29 06	53.0	TS/TD	20.0	49	NP	NP
68	Earl	2010-08-29 18	2010-08-30 06	80.0	Cat. 1	40.0	49	P	P
69	Earl	2010-08-30 06	2010-08-30 12	100.0	Cat. 3	15.0	26	P	P
70	Earl	2010-08-30 12	2010-08-30 18	110.0	Cat. 3	0.0	22	P	P
71	Earl	2010-08-30 18	2010-08-31 00	115.0	Cat. 4	-5.0	42	NP	NP
72	Earl	2010-08-31 15	2010-09-01 07	110.0	Cat. 3	0.0	12	NP	P
73	Earl	2010-09-01 07	2010-09-01 20	111.6	Cat. 3	20.0	20	NP	NP
74	Earl	2010-09-01 18	2010-09-02 06	120.0	Cat. 4	-10.0	27	P	NP
75	Earl	2010-09-02 06	2010-09-02 18	113.3	Cat. 4	-50.0	19	NP	NP

This article is protected by copyright. All rights reserved.

76	Earl	2010-09-02 22	2010-09-03 13	90.0	Cat. 2	-30.0	34	NP	NP
77	Earl	2010-09-03 13	2010-09-04 03	68.3	Cat. 1	-20.0	42	NP	NP
78	Bill	2009-08-19 20	2009-08-20 02	115.0	Cat. 4	-20.0	22	NP	NP
79	Bill	2009-08-20 08	2009-08-20 13	105.0	Cat. 3	10.0	21	NP	NP
80	Hilary	2011-09-28 17	2011-09-28 20	70.0	Cat. 1	-20.0	27	P	NP
81	Hilary	2011-09-29 16	2011-09-29 19	50.0	TS/TD	-40.0	16	P	P
82	Rina	2011-10-26 23	2011-10-27 02	80.0	Cat. 1	-40.0	23	NP	NP
83	Isaac	2012-08-26 20	2012-08-27 01	50.0	TS/TD	10.0	26	NP	NP
84	Isaac	2012-08-28 11	2012-08-28 15	65.0	Cat. 1	10.0	24	NP	P
85	Isaac	2012-08-28 20	2012-08-29 08	70.0	Cat. 1	-10.0	34	NP	NP
86	Isaac	2012-08-27 04	2012-08-27 17	58.3	TS/TD	10.0	24	P	P
87	Isaac	2012-08-27 16	2012-08-28 03	58.3	TS/TD	10.0	34	NP	NP
88	Sandy	2012-10-25 21	2012-10-26 00	75.0	Cat. 1	-20.0	11	NP	NP
89	Sandy	2012-10-26 00	2012-10-26 04	65.0	Cat. 1	-20.0	14	NP	NP
90	Sandy	2012-10-26 09	2012-10-26 14	65.0	Cat. 1	-10.0	21	NP	NP
91	Sandy	2012-10-27 08	2012-10-27 14	70.0	Cat. 1	-10.0	27	NP	NP

Table 2. Parameter limits for the pressure fit using the piece-wise function of Willoughby *et al.* (2006). For the profile inside the radius of maximum wind,  $n$  is the degree of the polynomial and  $V_{max}$  and  $R_{max}$  are the maximum wind speed and radius of maximum wind, respectively.  $L_1$  and  $L_2$  are length scales that constrain the exponential function outside the radius of maximum wind, and  $R_1$  and  $R_2$  are the radial distances that determine where the inner, transition and outer profiles are defined.

Parameter	Lower limit	Upper limit	Unit
$n$	1	1.5	N/A
$L_1$	420	700	km
$L_2$	15	35	km
$R_1$	RMW - (RMW/2)	RMW	km
$R_2$	RMW	2 RMW	km
$R_{max}$	RMW-2	RMW+2	km
$V_{max}$	$V_{max} - 10$	$V_{max} + 10$	$m s^{-1}$

Table 3. Statistical information of each composite of inner-core observations reporting the: mean and standard deviation and the p-value of a Welch and Kolmogorov-Smirnov (KS) statistical tests. Each test compared each composite to the *Control* sample, which includes all inner-core observations. The probabilities  $p$  of the agradient wind being higher than  $15 m s^{-1}$  and lower than  $-15 m s^{-1}$  in each distribution are also shown.

Composite	Mean	st dev	p-value (Welch)	p-value (KS)	$p(V_{ag} < -15m s^{-1})$	$p(V_{ag} > 15m s^{-1})$
<i>Control</i>	1.3	12.1	-	-	0.07	0.11
Intensifying	1.08	11.8	> 0.05	< 0.05	0.08	0.11
Weakening	1.5	12.6	> 0.05	> 0.05	0.08	0.14
Steady-state	0.8	8.7	> 0.05	< 0.05	0.03	0.07
TS/TD	-1.0	8.0	> 0.05	< 0.01	0.05	0.05
Cat. 1	-2.4	8.5	< 0.01	< 0.01	0.07	0.03
Cat. 2	0.1	10.7	< 0.05	< 0.01	0.1	0.06
Cat. 3	3.0	11.0	< 0.01	< 0.01	0.06	0.14
Cat. 4,5	3.9	12.8	< 0.01	< 0.01	0.07	0.19
Flat	0.3	11.2	< 0.01	< 0.01	0.09	0.09
Peaked	3.4	13.5	< 0.01	< 0.01	0.07	0.19
400-600 m	2.6	12.7	< 0.01	< 0.01	0.08	0.16
>1500 m	-0.7	11.0	< 0.01	< 0.01	0.1	0.08